Intermediate-mass-ratio black hole binaries. II. Modeling trajectories and gravitational waveforms

Hiroyuki Nakano, Yosef Zlochower, Carlos O. Lousto, and Manuela Campanelli

Phys. Rev. D **84**, 124006 — Published 2 December 2011

DOI: 10.1103/PhysRevD.84.124006

Intermediate-mass-ratio black hole binaries II: Modeling Trajectories and Gravitational Waveforms

Hiroyuki Nakano, Yosef Zlochower, Carlos O. Lousto, Manuela Campanelli
Center for Computational Relativity and Gravitation, and School of Mathematical Sciences, Rochester Institute of Technology, 85 Lomb Memorial Drive, Rochester, New York 14623

We revisit the scenario of small-mass-ratio (q) black-hole binaries; performing new, more accurate, simulations of mass ratios 10:1 and 100:1 for initially nonspinning black holes. We propose fitting functions for the trajectories of the two black holes as a function of time and mass ratio (in the range $1/100 \leq q \leq 1/10$) that combine aspects of post-Newtonian trajectories at smaller orbital frequencies and plunging geodesics at larger frequencies. We then use these trajectories to compute waveforms via black hole perturbation theory. Using the advanced LIGO noise curve, we see a match of $\sim 99.5\%$ for the leading $(\ell, m) = (2, 2)$ mode between the numerical relativity and perturbative waveforms. Nonleading modes have similarly high matches. We thus prove the feasibility of efficiently generating a bank of gravitational waveforms in the intermediate-mass-ratio regime using only a sparse set of full numerical simulations.

PACS numbers: 04.25.dg, 04.30.Db, 04.25.Nx, 04.70.Bw

I. INTRODUCTION

Numerical relativity (NR) has come a long way since the breakthroughs of 2005 [1–3] that allowed, for the first time, long-term evolution of black hole binaries (BHBs). Among NR's significant achievements are its contributions towards the modeling of astrophysical gravitational wave sources that will be relevant for the first direct detection and parameter estimation by gravitational wave observatories [4]. NR has also made contributions to the modeling of astrophysical sources, notably with the discovery of very large recoil velocities [5–8], and the application of the numerical techniques to combined systems of BHs and neutron stars [9]. More mathematical aspects of relativity have also recently been investigated, including the evolution of N-black holes [10], the exploration of the no-hair theorem [11, 12], and cosmic [13] and topological censorship [14], as well as BHBs in dimensions higher than four [15].

Among the remaining challenges are the exploration of the extremes of the BHB parameter space. The current state of the art simulations can simulate BHBs with mass ratios as small as $q = 1/100$ [16, 17] and highly spinning BHBs with intrinsic spins $\alpha = S_H/M_H^2$ up to (at least) 0.97 [18, 19]. Currently these runs are very costly and it is hard to foresee the possibility of completely covering the parameter space densely enough for match filtering the data coming from advanced laser interferometric detectors by the time they become operational. It is therefore imperative to develop interpolation techniques that allow for astrophysical parameter estimations, at a reasonable level of accuracy, based on a sparse set of numerical simulations.

In this spirit, we designed a set of prototypical runs for initially non spinning BHBs with small mass ratios q in the range $0.1 \leq q \leq 0.01$. Since we expect that, for small enough mass ratios, this BHB system will be describable by perturbation theory, we compare the full numerical waveforms with those produced by perturbative evolutions via the Regge-Wheeler [20] and Zerilli [21] equations, supplemented by linear corrections in the spin of the large BH [22]. The key ingredients perturbation theory needs is the relative trajectory of the small BH with respect to the larger one and the background mass and spin. In our previous tests we used the full numerical tracks and proved the perturbative waveforms agree reasonably well with the full numerical ones [22]. In this paper we develop a model with free fitting parameters for these trajectories based on post-Newtonian (PN) and geodesic input, and fit to full numerical tracks. For these fits, we use full numerical evolutions of $q = 1/10$ and $q = 1/100$ BHBs [16, 22] and perform new, more accurate simulations. We compare the waveforms for the modeled tracks with the full numerical waveforms to confirm matching agreement within a fraction of a percent. Hence this method paves the way for further generalizations and simulations to provide an approximate, yet accurate, bank for waveforms for second generation gravitational wave detectors.

This paper is organized as follows. In Sec. II we review the numerical methodology to perform the small mass ratio runs. In Sec. III we describe the runs and results. In Sec. IV we describe the track modeling on PN expansions and fits to the full numerical results. In Sec. V we give the results of using those tracks to generate perturbative waveforms and compares them with those extracted from the full numerical evolutions. We discuss the consequences and future application of this techniques in Sec. VI. We also include an appendix A to briefly discuss perturbative theory in numerical coordinates (1+log, trumpet coordinates).

II. NUMERICAL RELATIVITY TECHNIQUES

To compute the numerical initial data, we use the puncture approach [23] along with the TwoPunctures [24] thorn. In this approach the 3-metric on the initial slice has the form $\gamma_{ab} = (\psi_{BL} + u)^4 \delta_{ab}$, where ψ_{BL} is the Brill-Lindquist conformal factor, δ_{ab} is the Euclidean metric, and u is (at least) C^2 on the punctures. The Brill-Lindquist conformal factor is given by $\psi_{BL} = 1 + \sum_{i=1}^{n} m_i^p/(2|\vec{r} - \vec{r}_i|)$, where n is the total number of 'punctures', m_i^p is the mass parameter of puncture i (m_i^p is *not* the horizon mass associated with puncture i), and $\vec{r}_i$ is the coordinate location of puncture i. We evolve these black-hole-binary data-sets using the LazEv [25] implementation of the moving puncture approach [2, 3] with the conformal function $W = \sqrt{\chi} = \exp(-2\phi)$ suggested by Ref. [26]. For the runs presented here, we use centered, eighth-order finite differencing in space [10] and a fourth-order Runge-Kutta time integrator. (Note that we do not upwind the advection terms.)

Our code uses the Cactus/EinsteinToolkit [27, 28] infrastructure. We use the Carpet [29] mesh refinement driver to provide a "moving boxes" style of mesh refinement. In this approach refined grids of fixed size are arranged about the coordinate centers of both holes. The Carpet code then moves these fine grids about the computational domain by following the trajectories of the two BHs.

We use AHFinderDirect [30] to locate apparent horizons. We measure the magnitude of the horizon spin using the Isolated Horizon algorithm detailed in Ref. [31]. Note that once we have the horizon spin, we can calculate the horizon mass via the Christodoulou formula

$$m^H = \sqrt{m_{\rm irr}^2 + S^2/(4m_{\rm irr}^2)}, \qquad (1)$$

where $m_{\rm irr} = \sqrt{A/(16\pi)}$ and A is the surface area of the horizon. We measure radiated energy, linear momentum, and angular momentum, in terms of ψ_4, using the formulae provided in Refs. [32, 33]. However, rather than using the full ψ_4, we decompose it into ℓ and m modes and solve for the radiated linear momentum, dropping terms with $\ell \geq 5$. The formulae in Refs. [32, 33] are valid at $r = \infty$. Typically, we would extract the radiated energy-momentum at finite radius and extrapolate to $r = \infty$. However, for the smaller mass ratios examined here, noise in the waveform introduces spurious effects that make these extrapolations inaccurate. We therefore use the average of these quantities extracted at radii $r = 70$, 80, 90, 100 and use the difference between these quantities at different radii as a measure of the error.

We extrapolate the waveform to $r \to \infty$ using the perturbative formula [22]

$$\lim_{r\to\infty} [r\,\psi_4^{\ell m}(r,t)] = \left[r\,\psi_4^{\ell m}(r,t) - \frac{(\ell-1)(\ell+2)}{2} \int_0^t dt\,\psi_4^{\ell m}(r,t) \right]_{r=r_{\rm Obs}} + O(R_{\rm Obs}^{-2}), \qquad (2)$$

where $r_{\rm Obs}$ is the approximate areal radius of the sphere $R_{\rm Obs} = const.$ We have found that this formula gives reliable extrapolations for $R_{\rm Obs} \gtrsim 100M$. We note that Eq. (2) assumes the Weyl scalar is calculated in the Kinnersley tetrad. When using the Psikadelia tetrad, one needs to multiply the RHS of Eq. (2) by a factor of $((1/2 - M/r)$, which accounts for the difference in normalization (at infinity) between the two tetrads.

Recent Cauchy-Characteristic extraction (CCE) studies [34] (see also Ref. [35]) showed that this perturbative extrapolation formula can be more accurate than a linear extrapolation of the waveforms at finite radius to infinite resolution (provided that the observer R is in the far zone). Those studies compared the extrapolated waveforms with the gauge invariant waveform on $\mathscr{I}^+$ obtained using a nonlinear characteristic evolution from a finite radius to $\mathscr{I}^+$ along outgoing null slices. The authors of Ref. [34] measured the errors in $r\psi_4$ for an equal-mass BHB simulation when extracting at $R = 50M$ and $R = 100M$, the corresponding extrapolation to ∞, as well as the error in $r\psi_4$ obtained by applying the perturbative extrapolation formula (2) to the $R = 100M$ waveform. The errors in the perturbative extrapolation where the smallest over the entire waveform (both in amplitude and phase).

We note that multi-patch [36] and pseudospectral [37] techniques allow extraction radii very far from the source, leading to very small extrapolation errors.

A. Gauge

We obtain accurate, convergent waveforms and horizon parameters by evolving this system in conjunction with a modified 1+log lapse and a modified Gamma-driver shift condition [2, 38], and an initial lapse $\alpha(t = 0) = 2/(1 + \psi_{BL}^4)$. The lapse and shift are evolved with

$$(\partial_t - \beta^i \partial_i)\alpha = -2\alpha K, \qquad (3a)$$

$$\partial_t \beta^a = (3/4)\tilde{\Gamma}^a - \eta(x^a, t)\beta^a, \qquad (3b)$$

where different functional dependencies for $\eta(x^a, t)$ have been proposed in Refs. [25, 39–43]. Here we use a modification of the form proposed in Ref. [40],

$$\eta(x^a, t) = R_0 \frac{\sqrt{\partial_i W \partial_j W \tilde{\gamma}^{ij}}}{(1 - W^a)^b}, \qquad (4)$$

where we chose $R_0 = 1.31$. The above gauge condition is inspired by, but differs from Ref. [40] between the BHs and in the outer zones when $a \neq 1$ and $b \neq 2$. Once the conformal factor settles down to its asymptotic $\psi = C/\sqrt{r} + O(1)$ form near the puncture, η will have the form $\eta = (R_0/C^2)(1 + b(r/C^2)^a)$ near the puncture and $\eta = R_0 r^{b-2} M/(aM)^b$ as $r \to \infty$. In practice we used $a = 2$ and $b = 2$, which reduces η by a factor of 4 at infinity when compared to the original version of this gauge proposed by Ref. [40]. We note that if we set $b = 1$

TABLE I: Initial data parameters for the numerical simulations. Note that the $q = 1/15$ simulations are older and used a CFL factor twice as large. Here m_1^p and m_2^p are the two puncture mass parameters, the puncture were located at $(x_1, 0, 0)$ and $(x_2, 0, 0)$ with momentum $\pm(P_r, P_t, 0)$ and zero spin. The measured horizon masses and total ADM mass are also provided.

Param	$q = 1/10$	$q = 1/15$	$q = 1/100$
m_1^p	0.085237276	0.057566227	0.0086894746
m_2^p	0.907396855	0.936224183	0.9896192142
x_1	7.633129115	6.806172805	4.952562636
x_2	-0.7531758055	-0.4438775230	-0.04743736368
P_t	0.0366988	0.0290721	0.00672262416584
P_r	-0.000168519	-0.000160518	-0.00001026521884
m_{H1}	0.09129	0.06254	0.99065
m_{H2}	0.91255	0.94044	0.00990841
$M_{\rm ADM}$	1.00004	1.00005	1.00000000

then η will have a $1/r$ falloff at $r = \infty$ as suggested by Ref. [42]. Our tests indicate that the choices $(a = 2, b = 1)$ and $(a = 1, b = 1)$ lead to more noise in the waveform than $(a = 2, b = 2)$.

III. SIMULATIONS AND RESULTS

The initial data parameters for the $q = 1/10$, $q = 1/15$, and $q = 1/100$ simulations are given in Table I. Note that the $q = 1/15$ simulations are older and suffer from the mass loss error discussed below.

We used a base (coarsest) resolution of $h_0 = 4M$ with 11 levels of refinement for $q = 1/10$ simulations and 15 levels of refinement for $q = 1/100$ for the low resolution simulations. The outer boundaries were at $400M$. The higher resolution simulations were all based on these grids, but with correspondingly more gridpoints per level. The grid structure was chosen by studying the behavior of the background potential for the propagation of perturbations [16]. In the appendix A we show this potential, both in the isotropic coordinates of the initial data and final 'trumpet' coordinates.

We previously evolved a set of $q = 1/10$, $q = 1/15$ [22], and $q = 1/100$ [16] BHBs using the standard choice of Courant-Friedrichs-Lewy (CFL) factor $dt/h \sim 0.5$. Although we found the waveform at lower resolution appear to converge, an unphysical mass loss led to incorrect dynamics at later times (see Fig. 1). This, in turn, led to oscillations in the errors as a function of grid resolution h. We found that reducing the CFL factor significantly reduces these unphysical effects [71]. In Figs. 1 and 2 we plot the horizon mass as a function of time for three resolutions using both the old and new CFL factor for both the $q = 1/10$ and $q = 1/100$ simulations. Note the much better conservation of the mass and the corresponding reduction in the lifetime of binary. PN trajectory evolutions (see Fig. 3) indicate that the mass losses as small as 1 part in 10^4 are dynamically important, and the error introduced by this mass loss is significantly reduced by the new integration. The effects of the time integrator on the numerical error, and in particular the mass loss and constraint violation errors, will be the subject of an upcoming paper by Ponce, Lousto, and Zlochower.

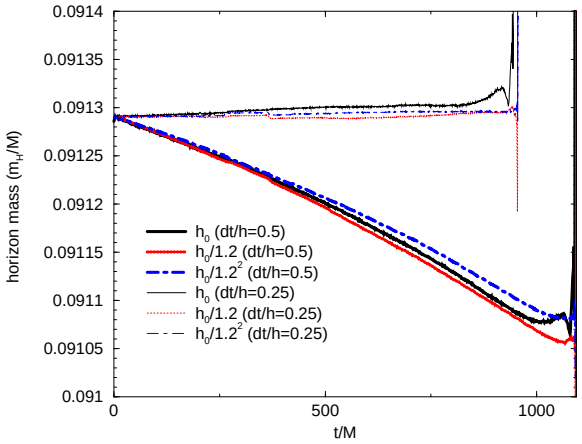

FIG. 1: The horizon mass conservation using CFL factors of 0.5 and 0.25 for the $q = 1/10$ simulations. A factor of 10 better results are obtained using a CFL factor of 0.25. The effect on the trajectory is significant because the mass loss is dynamically important (it significantly delays the merger). The mass changes post merger (sharp spikes near $t \sim 950M$ and $t \sim 1080M$) are not dynamically important.

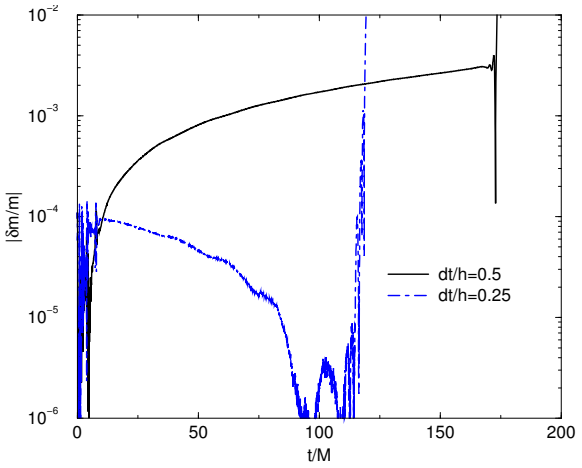

FIG. 2: The horizon mass conservation using CFL factors of 0.5 and 0.25 for the $q = 1/100$ simulations. Here $|\delta m|$ is the absolute value of the difference between the expected horizon mass and the measured horizon mass for the smaller BH. In the case of $q = 1/100$, as in the case of $q = 1/10$, the horizon mass decreases (hence $|\delta m|$ increases) with time when using a CFL factor of 0.5. A factor of 20 better results are obtained using a CFL factor of 0.25. The effect on the trajectory is significant because the mass loss is dynamically important (it delays the merger). The mass changes post merger (sharp spikes near $t = 115M$ and $t = 172M$) are *not* dynamically important.

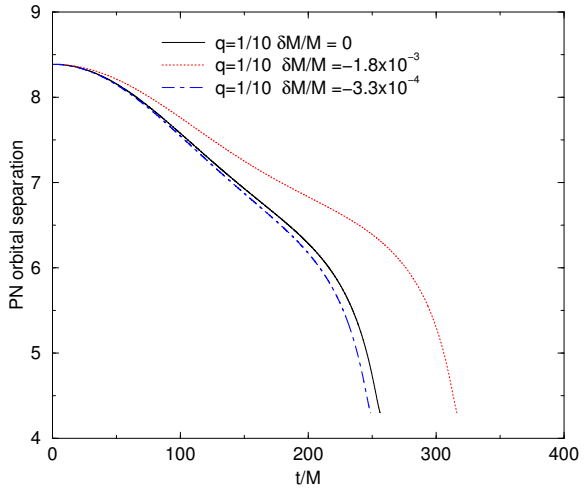

FIG. 3: The 3.5PN orbital separations for the $q = 1/10$ binary (the eccentricity is due to the fact that we use identical parameters as the full numerical simulation, which are not quasi-circular PN parameters) for slightly different small BH masses. A mass loss of 1 part in 10^4 is dynamically important, leading to a significantly delayed merger. Reducing the mass change by a factor of 10 significantly reduces this error.

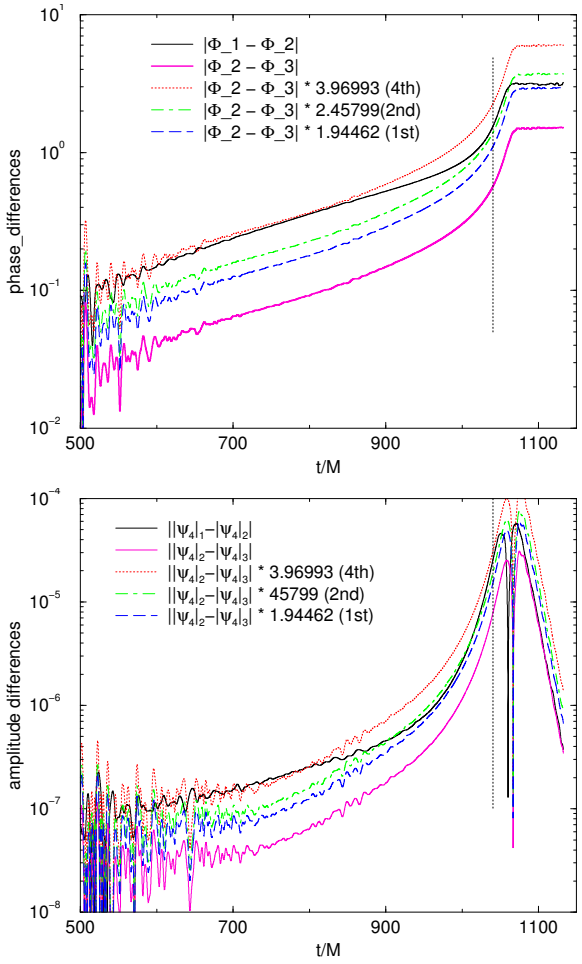

FIG. 4: Convergence of the $(\ell = 2, m = 2)$ mode of ψ_4 for the $q = 1/10$ waveform. The waveform starts out fourth-order accurate (due to our fourth-order waveform extraction algorithm), but then reduces to second order during the late inspiral, and dropping to first-order during the ringdown. The vertical line indicates the time when the frequency is $\omega = 0.2/M$. The central resolutions for the three cases were $h_1 = M/256$, $h_2 = M/337.9$, and $h_3 = M/404.48$, respectively, and each configuration used 11 levels of refinement.

For the $q = 1/10$ nonspinning BHB, we performed simulations with central resolutions of $h = M/256$, $h = M/307.2$, $M/337.9$, $M/368.64$, and $M/404.48$, with 11 levels of refinement in each case (the coarsest grid resolutions where h_0, $h_0/1.2$, $h_0/1.32$, $h_0/1.44$, $h_0/1.58$, respectively). We note that the waveform showed oscillations in error as a function of resolution. We are therefore using the most widely spaced (in resolution) runs for the convergence plot. In particular, we use the $h = M/256$, $M/337.9$, and $M/404.48$ simulations.

In Fig. 4 we show the convergence of the amplitude and phase of ψ_4 for these three resolutions. Convergence appears to break just at the start of the final plunge. Figure 5 shows the highest resolution waveform and the Richardson extrapolation (assuming a second-order error). The extrapolation error becomes large just near the plunge, at a frequency of $\omega = 0.19/M$. We also plot the phase deference between the highest resolution run and the Richardson extrapolated waveform. The vertical line shows the point when the frequency is $\omega = 0.2/M$. The phase error, up to $t = 850M$ is within 0.04 radian, but increases exponentially to 1.2 radians when $\omega = 0.2/M$.

Determining convergence for the $q = 1/100$ simulations proved challenging for two reasons. There was a small random jump in the mass of the smaller BH between resolutions that had a small effect on the trajectory. From Fig. 6 we can see a difference of one part in 10^4 in the small BH mass. The two medium resolution have lower masses, and therefore merge slightly later than expected. The net effect is to confuse the order when the mergers happens (we expected the higher resolutions runs to merge slightly later than the lower resolutions runs). We see from Fig. 7 that the second-lowest resolution merges out of order with the other runs. Similarly, the third lowest resolution appears to merge late, as well. Another source of confusion for our convergence study has to do with lower-order errors (not necessarily associated with the mass) becoming important at higher resolutions. This leads to oscillations in the error as a function of resolution that can cause the merger time to oscillate with resolution. Nevertheless, the actual deviations in the trajectories, for the higher resolutions, is small. The improvement over the original $q = 1/100$ simulation is substantial. The mass conservation is a factor of 20 better. The old simulations had an unphysical extra orbit inside the ISCO due to significant mass loss. Convergence measurements of the waveform do not appear to suffer much from the above

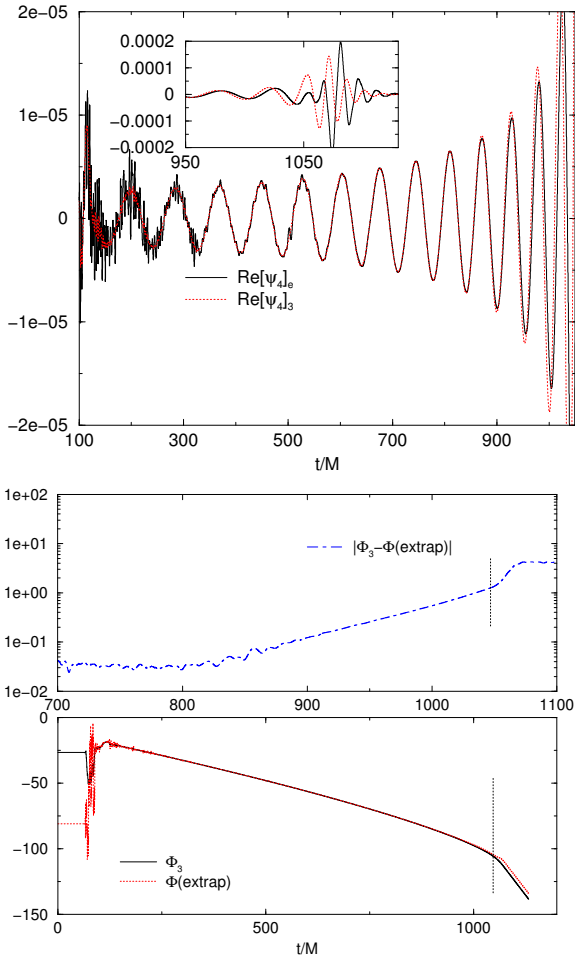

FIG. 5: (TOP) A comparison of the highest resolution run with the Richardson extrapolated waveform. At the plunge, the phase error in the waveform is sufficiently large that the extrapolation give erroneous results (note the unphysical oscillation near $t = 1050M$). The extrapolation breaks down at $\omega = 0.19/M$. (BOTTOM) The phase difference between the Richardson extrapolated waveform and the highest resolution.

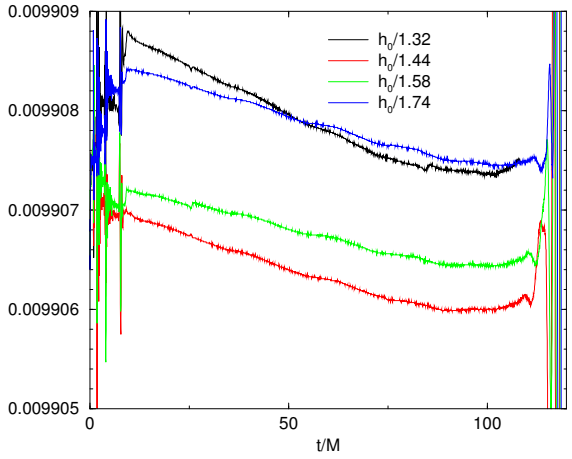

FIG. 6: The horizon mass for the $q = 1/100$ configurations. Jumps in the horizon mass of order $1/10^4$ are apparent between resolutions. this has a small but noticeable dynamic effect.

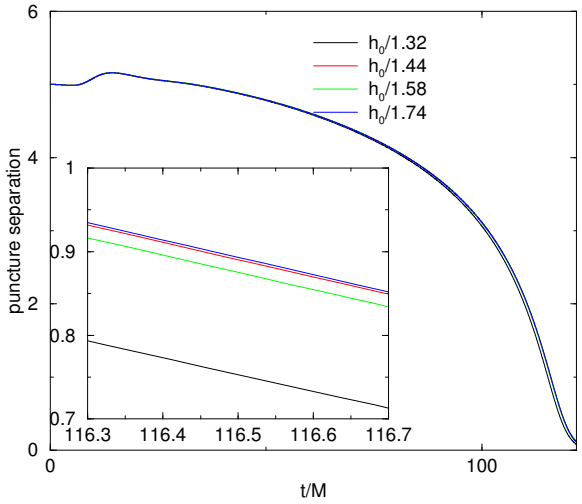

FIG. 7: The puncture separation as a function of time for the $q = 1/100$ configurations. The second lowest resolution run appears to merge later than expected, consistent with its reduced mass (apparent in Fig. 6)

mentioned mass loss. However, due to low amplitude of the waveform compared to the grid noise (induced by the refinement boundaries), the differences in the waveforms at the various resolution were smaller than the grid-noise fluctuations. Figures 9 and 10 show the waveform and phase for the three highest resolutions. Note that the gridnoise apparent in Fig. 9 is due to reflections of the initial data pulse at the refinement boundaries. For our configuration, the imaginary part of the $(\ell = 2, m = 2)$ components of this pulse is small compared to the real part. This leads to a significant reduction (about a factor of 10) in the noise in the imaginary part when compared to the real part. Figure 8 shows the trajectories for the four highest resolutions. Note that good agreement between the curves when using the new smaller CFL factor.

For reference, we report the final remnant properties for the three configurations in Table II.

The above gauge conditions (3) have a drawback near merger. The conformal function W goes to zero at the two punctures and there is a local maximum between the two punctures. Due to this local maximum, $\eta \to 0$ at some point between the two punctures. As the two punctures approach each other, this zero in η get progressively closer to the smaller BH. This, in turn, causes the coordinate radius of the horizon to shrink near merger. As seen in Fig. 11, the horizon radius for the new $q = 1/100$ simulations decreases at merger, leading to a loss in resolution of the smaller BH. Another issue related to this gauge is that the relative effective size (i.e. r_H/m_H) of the smaller BH is less than that of the larger BH. So the

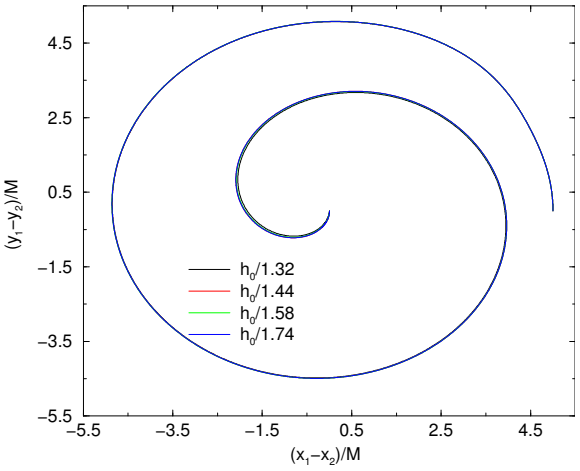

FIG. 8: The puncture trajectories for the $q = 1/100$ configuration.

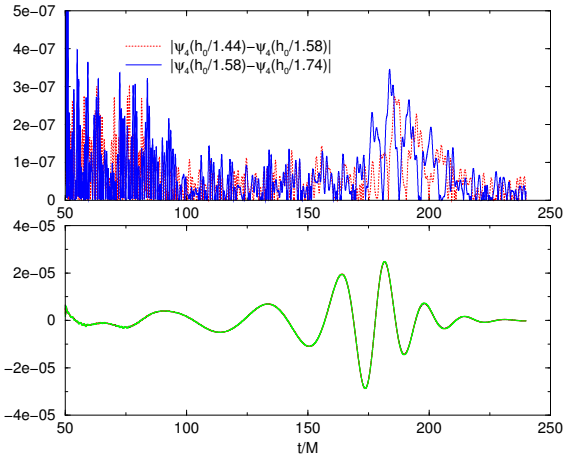

FIG. 9: The imaginary part (which is much less noisy than the real part) of the $(\ell = 2, m = 2)$ mode of ψ_4 for the $q = 1/100$ configurations. The differences in waveform between resolutions are dominated by grid noise at high resolutions. At the peak, the differences in the waveforms between resolutions is about 1% of the amplitude of the waveform. The real part of the waveform is roughly a factor of 10 more noisy.

required resolution (gridpsacing) for each hole does not scale exactly with the BH's mass. This lower effective relative size of the smaller BH may be partially responsible for the reduced conservation of the horizon mass of the smaller BH when compared to the larger on (see Fig. 12).

IV. PERTURBATIVE TECHNIQUES

In Ref. [22], we extended the Regge-Wheeler-Zerilli (RWZ) formalism [20, 21] of black hole perturbation theory to include, perturbatively, a term linear in the spin of the larger BH. This Spin-Regge-Wheeler-Zerilli

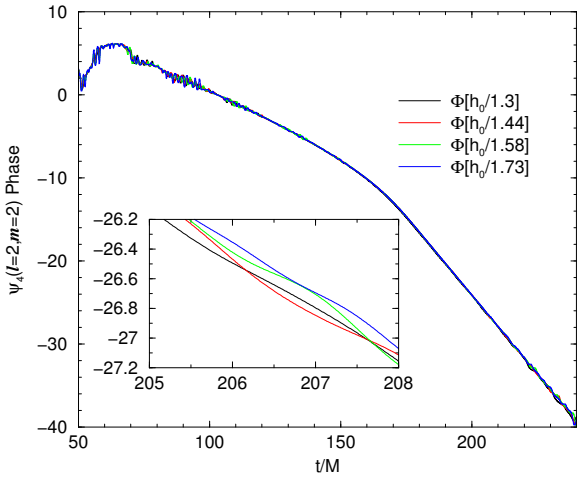

FIG. 10: The phase of the $(\ell = 2, m = 2)$ mode of ψ_4 for the $q = 1/100$ configurations. The differences in phases between resolutions are dominated by grid noise.

TABLE II: Final remnant intrinsic spin, radiated energy, and recoil velocity for the $q = 1/10$, $q = 1/15$, and $q = 1/100$ configurations. For reference we also include the predicted recoil velocity based on [44].

Param	$q = 1/10$	$q = 1/15$	$q = 1/100$
α	0.261 ± 0.002	0.189 ± 0.006	0.0332 ± 0.0001
$E_{\rm rad}/M$	0.0044 ± 0.0001	0.0022 ± 0.0001	$(5.5 \pm 1.0) \times 10^{-5}$
$V_{\rm kick}$	60 ± 2 km s^{-1}	34 ± 2 km s^{-1}	1.0 ± 0.1 km s^{-1}
$V_{\rm pred}$	62 km s^{-1}	34 km s^{-1}	1.1 km s^{-1}

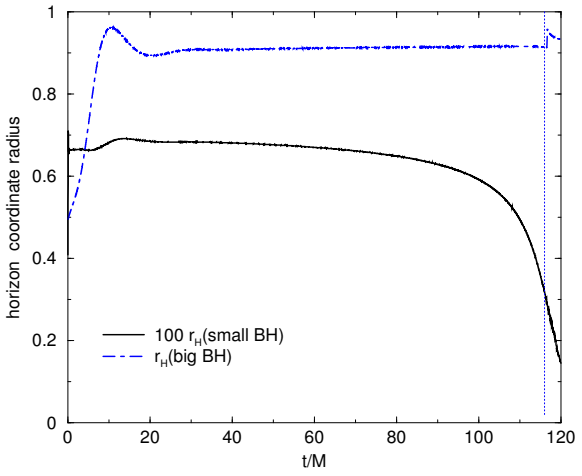

FIG. 11: The horizon radius of both BHs for the new $q = 1/100$ simulations. The horizon radius of the larger BH barely changes, while the radius of the smaller BH decreases sharply at merger.

(SRWZ) formalism has second-order perturbations with linear dependence on the spin in the wave equations for Schwarzschild perturbations.

In the SRWZ formalism, the wave functions for the

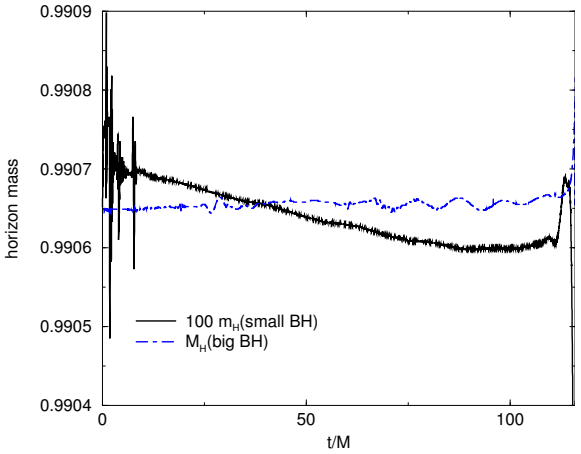

FIG. 12: The horizon mass of both BHs for the new $q = 1/100$ simulations. The horizon mass of the larger BH is conserved to a higher degree than that of the smaller BH. This is the case even though the number of gridpoints inside the smaller BH is actually larger than the number of gridpoints in the larger BH.

even and odd parity perturbations are expressed as a combined wave function of the first and second perturbative orders,

$$\begin{aligned}\Psi_{\ell m}(t,r) &= \Psi^{(1)}_{\ell m}(t,r) + \Psi^{(2)}_{\ell m}(t,r)\,, \\ \Psi^{(\rm o)}_{\ell m} &= \Psi^{(\rm o,1)}_{\ell m} + 2\int dt\,\Psi^{(\rm o,Z,2)}_{\ell m}\,, \end{aligned} \tag{5}$$

where the superscript 1 and 2 denote the perturbative order, $\Psi_{\ell m}$ denotes the even parity Zerilli function, and $\Psi^{(\rm o,1)}_{\ell m}$ and $\Psi^{(\rm o,Z,2)}_{\ell m}$ denote the Regge-Wheeler (Cunningham et al.) and the Zerilli functions for the odd parity perturbations (see Ref. [45] for the relation between the wave functions). These functions satisfy the following three equations.

$$\begin{aligned}
&-\frac{\partial^2}{\partial t^2}\Psi_{\ell m}(t,r) + \frac{\partial^2}{\partial r^{*2}}\Psi_{\ell m}(t,r) \\
&\quad -V^{(\rm even)}_{\ell}(r)\Psi_{\ell m}(t,r) + i\,m\,\alpha\,\hat{P}^{(\rm even)}_{\ell}\Psi_{\ell m}(t,r) \\
&= S^{(\rm even)}_{\ell m}(t,r;r_p(t),\phi_p(t))\,, \\
&-\frac{\partial^2}{\partial t^2}\Psi^{(\rm o,1)}_{\ell m}(t,r) + \frac{\partial^2}{\partial r^{*2}}\Psi^{(\rm o,1)}_{\ell m}(t,r) \\
&\quad -V^{(\rm odd)}_{\ell}(r)\Psi^{(\rm o,1)}_{\ell m}(t,r) \\
&= S^{(\rm odd,1)}_{\ell m}(t,r;r_p(t),\phi_p(t))\,, \\
&-\frac{\partial^2}{\partial t^2}\Psi^{(\rm o,Z,2)}_{\ell m}(t,r) + \frac{\partial^2}{\partial r^{*2}}\Psi^{(\rm o,Z,2)}_{\ell m}(t,r) \\
&\quad -V^{(\rm odd)}_{\ell}(r)\Psi^{(\rm o,Z,2)}_{\ell m}(t,r) \\
&= S^{(\rm odd,Z,2)}_{\ell m}(t,r;r_p(t),\phi_p(t))\,,
\end{aligned} \tag{6}$$

where $r^* = r + 2M\ln[r/(2M) - 1]$ is a characteristic coordinate, α is the non-dimensional spin parameter, $V^{(\rm even/odd)}_{\ell}$ denotes the Zerilli and Regge-Wheeler potential, respectively, $S_{\ell m}$ is the source term, and $(r_p(t), \phi_p(t))$ are the particle separation and orbital phase as a function of time. The differential operator $\hat{P}^{(\rm even)}_{\ell}$ arises from the coupling between the BH's spin and the first-order wave functions. We note that $S^{(\rm even)}_{\ell m}$ and $S^{(\rm odd,Z,2)}_{\ell m}$ include local and extended source terms arising from the second perturbative order associated with products of terms linear in α and the first-order perturbation functions. See Appendix A in Ref. [22] for more details.

In order to evolve the perturbative equations (6), we need the particle trajectory $(r_p(t), \phi_p(t))$ as a function of time. Here we use a PN inspired model for the BH trajectories, which will approximate the numerical trajectories from intermediate-mass-ratio BHB inspirals. In order to model the numerical trajectories for the late inspiral phase of a BHB merger using a relatively straightforward fitting function, we start with an adiabatic quasicircular evolution, i.e., ignoring the eccentricity of the orbit and the component of radial velocity not due to the radiation reaction, and then parametrize deviations from a 3.5PN-TaylorT4 adiabatic inspiral. We model the time derivative of the orbital frequency $d\Omega/dt$ and the orbital separation R as a function of the orbital frequency Ω based on an extension of standard PN calculations, described below.

A. The orbital frequency Ω evolution of the NR trajectories

First, we focus on the $d\Omega/dt$ evolution with respect to the orbital frequency Ω. In PN calculations for the quasicircular case, the evolution for Ω is obtained from the energy loss dE/dt and the relation between energy and frequency $E(\Omega)$ given by

$$\frac{d\Omega}{dt} = \frac{dE}{dt}\left(\frac{dE}{d\Omega}\right)^{-1}\,, \tag{7}$$

where dE/dt and $dE/d\Omega$ are obtained by appropriate PN expansions. In the TaylorT1 waveform, we simply substitute these quantities into Eq. (7). By expanding the TaylorT1 in the PN series again, we obtain the TaylorT4 waveform, which has been shown to give good agreement with numerical simulations [46]. Therefore, we develop a fitting function based on the TaylorT4 evolution. These Taylor series waveforms are summarized in Ref. [47].

We note here that for Schwarzschild geodesics, $d\Omega/dt$ diverges at the innermost stable circular orbit (ISCO), $R_{\rm Sch} = 6M$ in Schwarzschild coordinates. This is because $dE/d\Omega$ becomes zero at the ISCO frequency $M\Omega = (1/6)^{3/2} \sim 0.0680413817$. Although we need to develop techniques for the transition to plunge [48, 49] in the above situation, there is no divergence in the TaylorT4 waveform because the Taylor series expansion always has finite $d\Omega/dt$.

When fitting of the trajectories in the NR coordinates for various mass ratios, we use the following modified

TaylorT4 evolution.

$$
\begin{aligned}
\frac{d\Omega}{dt} &= \frac{96}{5}\,\Omega^{11/3} M^{5/3}\eta\,\left(1+B\,(\Omega/\Omega_0)^{\beta/3}\right)^{-1}\left(1+\left(-\frac{743}{336}-\frac{11}{4}\,\eta\right)(M\Omega)^{2/3}+4\,\pi\,M\Omega\right.\\
&+\left(\frac{34103}{18144}+\frac{13661}{2016}\,\eta+\frac{59}{18}\,\eta^2\right)(M\Omega)^{4/3}+\left(-\frac{4159}{672}\,\pi-\frac{189}{8}\,\eta\,\pi\right)(M\Omega)^{5/3}\\
&+\left(\frac{16447322263}{139708800}+\frac{16}{3}\,\pi^2-\frac{1712}{105}\,\gamma-\frac{1712}{315}\,\ln\left(64\,M\Omega\right)-\frac{56198689}{217728}\,\eta\right.\\
&\left.+\frac{451}{48}\,\eta\,\pi^2+\frac{541}{896}\,\eta^2-\frac{5605}{2592}\,\eta^3\right)(M\Omega)^2\\
&\left.+\left(-\frac{4415}{4032}\,\pi+\frac{358675}{6048}\,\eta\,\pi+\frac{91495}{1512}\,\eta^2\pi\right)(M\Omega)^{7/3}+A\,(\Omega/\Omega_0)^{\alpha/3}\right), \qquad (8)
\end{aligned}
$$

TABLE III: The summary of the fitting parameters for the "PN+" (a modification of the TaylorT4 evolution) in Eq. (8). The first line for the $q = 1/100$ case ($*$) gives the fitting parameters obtained by allowing all 4 constants to vary, the second line (†) for the $q = 1/100$ case gives the parameters from a fitting of A and B only by assuming $\alpha = 8$ and $\beta = 15$, and the third line (‡) gives the parameters extrapolated from the $q = 1/10$ and $q = 1/15$ results using Eq. (11).

Mass ratio	A	α	B	β
$q = 1/10$	17.0500	7.21975	8.18920	12.5197
$q = 1/15$	26.0150	7.54047	8.65525	13.6168
$q = 1/100^*$	93.0650	4.32071	5.42457	14.9711
$q = 1/100^\dagger$	288.888	8	16.2033	15
$q = 1/100^\ddagger$	233.985	9.45214	11.5411	21.0731

where $d\Omega/dt$ and Ω are obtained from the NR trajectories, and M and η denote the total mass and symmetric mass ratio of the binary system,

$$
\begin{aligned}
M &= m_1 + m_2\,, \\
\eta &= \frac{m_1 m_2}{M^2}\,, \qquad (9)
\end{aligned}
$$

respectively. Here, A, α, B and β are the fitting parameters, and the power in the parameters should be $\alpha > 7$ and $\beta > 7$ in order to be consistent with this (7/2)PN formula. Here Ω_0 is the frequency at $R_{\rm Sch} = 3M$ for circular orbits, i.e. $M\Omega_0 = (1/3)^{3/2} \sim 0.19245009$. In the fitting, we use the method of least squares.

In Table III, we summarize the parameters obtained from fitting for the three cases, $q = 1/10$, $q = 1/15$ (from Ref. [22]), and $q = 1/100$.

The fitting curve for the $q = 1/10$ case, which is valid up to $M\Omega = 0.175$, is shown in Fig. 13. The fitting parameters, α and β, for this case are consistent with the current PN formula, and we see that the fitting curve is close to the TaylorT4 evolution for small $M\Omega$.

FIG. 13: The fitting curve for the $q = 1/10$ case using Eq. (8) and orbital frequencies up to $M\Omega = 0.175$. The solid (black), dashed (red) and dotted (blue) curves show the NR, fitting and TaylorT4 PN evolutions, respectively. In the NR evolution, the end point of the solid (black) curve corresponds to $R_{\rm Sch} = 2M$, and $M\Omega = 0.175$ is the NR orbital frequency around $R_{\rm Sch} = 3M$, assuming the NR coordinate system can be approximated by a "trumpet" stationary 1 + log slice of the Schwarzschild spacetime. The inset shows the zoom-in of the initial part (around $M\Omega = 0.05$)

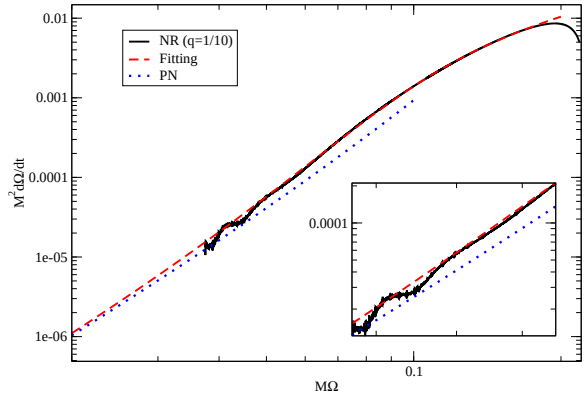

We show the fitting curve for the $q = 1/15$ case, which is valid up to $M\Omega = 0.17$, in Fig. 14. Again, the fitting parameters, α and β, for this case are consistent with the PN formula.

For the $q = 1/100$ case, which is shown in Fig. 15, we first found by a direct fit of all parameters that $\alpha < 7$, which is not consistent with the PN approach. One possibility is that the trajectories are too short. If we were to extend them to lower frequencies, we would expect that the slope increases, leading to a larger α. Below, we try two alternate fitting methods in order to try to improve the fit. This first fit gives the best agreement with the numerical trajectory so this is the one we use in Sec. V

FIG. 14: The fitting curve for the $q = 1/15$ case using Eq. (8) up to orbital frequencies of $M\Omega = 0.17$. The solid (black), dashed (red) and dotted (blue) curves show the NR, fitting and TaylorT4 PN evolutions, respectively. In the NR evolution, the end point of the solid (black) curve corresponds to $R_{\rm Sch} = 2M$, and $M\Omega = 0.17$ is the NR orbital frequency around $R_{\rm Sch} = 3M$, assuming the NR coordinate system can be approximated by a "trumpet" stationary $1 + \log$ slice of the Schwarzschild spacetime.

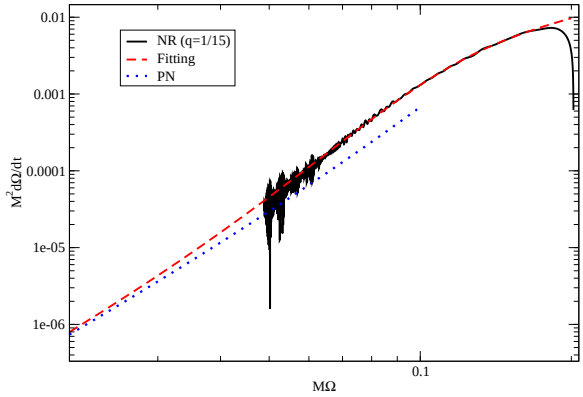

to calculate the gravitational waveforms. However, the second fit reproduces the expected behavior at large separations, so we expect that it gives a better waveform in that regime.

FIG. 15: The fitting curve for the $q = 1/100$ case using Eq. (8) with orbital frequencies up to $M\Omega = 0.15$. The solid (black) and dotted (blue) curves show the NR and TaylorT4 PN evolutions, respectively. The Fitting ($*$, dashed (red)), (1, dot-dashed (green)) and (2, dot-dot-dashed (magenta)) curves show the fitting curve with the ($*$), (†) and (‡) cases in Table III. In the NR evolution, $M\Omega = 0.15$ is the NR orbital frequency around $R_{\rm Sch} = 3M$, assuming the NR coordinate system can be approximated by a "trumpet" stationary 1+log slice of the Schwarzschild spacetime.

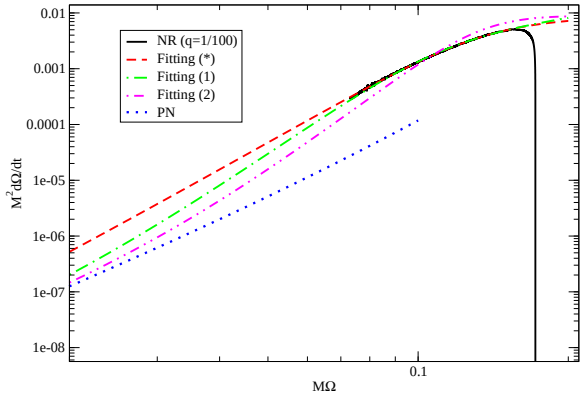

Note that, as seen in Fig. 15, the end point of the NR trajectory, which corresponds to $R_{\rm Sch} = 2M$, has $d\Omega/dt < 0$. This is a feature of Schwarzschild geodesics in Schwarzschild coordinates (e.g., a quasi-circular geodesic slightly inside the ISCO has $d\Omega/dt = -0.0113$). Hence it appears that in the $q = 1/100$ case the trajectories are much closer to geodesic motion than in the other cases.

Due to the fact that the $q = 1/100$ simulations were very short, obtaining accurate fitting parameters for the trajectory is error prone. As discussed in Ref. [50], longer NR simulations starting with a large orbital separation will be required to prevent inaccuracies of the PN Taylor-approximants in the late inspiral. We therefore consider several different techniques here. If we assume a simple fitting with respect to the mass ratio,

$$(A,\, \alpha,\, B,\, \beta) \;=\; c_0 \eta^{c_1}\,, \tag{10}$$

for the fitting parameters in the case of the $q = 1/10$ and $q = 1/15$ cases, we obtain

$$\begin{aligned} A &= 0.797021\,\eta^{-1.22855}\,, \\ \alpha &= 5.26843\,\eta^{-0.126379}\,, \\ B &= 5.48252\,\eta^{-0.160938}\,, \\ \beta &= 6.80971\,\eta^{-0.244245}\,. \end{aligned} \tag{11}$$

Then, inserting the symmetric mass ratio $\eta = 100/10201$ for $q = 1/100$ gives fitting parameters for $q = 1/100$. We report these values on the third line labeled $q = 1/100$ in Table III. The curve obtained by these parameters is denoted by "Fitting (2)" in Fig. 15. Note that these parameters actually produce a relatively poor fit for the trajectory. On the other hand, if we assume $\alpha = 8$ and $\beta = 15$ and fit the remaining parameters using the NR trajectory, we obtain the "Fitting (1)" parameters (second line labeled $q = 1/100$ in Table III). This fit smoothly interpolates between the PN trajectory at small frequencies and the start of the numerical trajectory at higher frequencies. Since both the standard fitting procedure, and "Fitting(1)" give reasonable fits, but different predictions, in order to accurately determine the constant in Eqs. (11), we need both more accurate and longer evolutions NR simulations of $q = 1/100$.

B. The orbital radius R versus orbital frequency Ω in the NR coordinates

In order to complete our description of the trajectories we need a fitting function that will allow us to express the separation R as a function of Ω. We use a function $R(\Omega)$ inspired by the ADM-TT PN approach [51], because the isotropic coordinates (used in the ADM-TT PN approach) and the radial isotropic "trumpet" stationary $1 + \log$ slices of the Schwarzschild spacetime are very similar [52, 53].

The fitting function based on the ADM-TT PN approach is given by

$$R = \frac{M}{(M\Omega)^{2/3}}\left(1+\left(-1+\frac{1}{3}\,\eta\right)(M\Omega)^{2/3}+\left(-\frac{1}{4}+\frac{9}{8}\,\eta+\frac{1}{9}\,\eta^2\right)(M\Omega)^{4/3}\right.$$
$$\left.+\left(-\frac{1}{4}-\frac{1625}{144}\,\eta+\frac{167}{192}\,\eta\,\pi^2-\frac{3}{2}\,\eta^2+\frac{2}{81}\,\eta^3\right)(M\Omega)^2\right)/\left(1+a_0(\Omega/\Omega_0)^{a_1}\right)+C\,, \quad (12)$$

TABLE IV: The fitting parameters for the "PN+" (a modification of the ADM-TT PN calculation) in Eq. (12) for the relation between R and Ω in the NR coordinates.

Mass ratio	C	a_0	a_1
$q=1/10$	0.216953	0.513214	4.68472
$q=1/15$	0.237427	0.600321	4.57899
$q=1/100$	0.198137	0.923360	5.29681

where R and Ω are in the NR coordinates, and a_0, a_1 and C are fitting parameters, and $M\Omega_0 = (1/3)^{3/2}$. Note that a_1 should be greater than 2 to be consistent with the PN calculation.

Initially, we expected that C, which is the difference between the NR radial coordinate and "trumpet" coordinate, would be very small because this term is inconsistent with the ADM-TT PN formula. However, we found that this term is non-trivial for all three mass-ratio cases.

The results of the fits are shown in Figs. 16-18 for $q = 1/10$, $q = 1/15$, and $q = 1/100$, respectively, and the fitting parameters are summarized in Table IV. We see from Table IV that the values of a_1 for all cases are consistent with the current PN calculation ($a_1 > 2$), and find a non-negligible $C \sim 0.2$ for all three cases. Due to this C contribution, there is a finite difference between the orbital radius evaluated in the ADM-TT PN approach and that by the fitting function in Eq. (12) even for smaller $M\Omega$.

As a result of the above fitting analysis, it is necessary to consider a radial transformation to remove the offset C between the NR coordinates ($R_{\rm NR} = R$ for Eq. (12)) and the "trumpet" coordinates,

$$R_{\rm NR} \to R_{\rm Log} = R_{\rm NR} - C\,. \quad (13)$$

After removing this offset, we then transform to the standard Schwarzschild coordinates, where the explicit time and radial coordinate transformations,

$$(T_{\rm Log},\, R_{\rm Log}) \to (T_{\rm Sch},\, R_{\rm Sch})\,, \quad (14)$$

are given in Ref. [54]. Here, we assume $T_{\rm NR} = T_{\rm Log}$. We note that after applying the C transformation discussed above, we find that the frequency when $R_{\rm Sch} = 3M$ is given by $M\Omega = 0.161$, 0.158 and 0.152 for the $q = 1/10$, $q = 1/15$ and $q = 1/100$ cases, respectively.

Note that this procedure of fitting NR trajectories directly in the NR coordinates and then transforming to Schwarzschild coordinates, appears simpler than the alternative of evolving the perturbations directly in the "trumpet" coordinate system. We nevertheless study this alternative in the Appendix A, where we provide the sourceless part of the perturbative equation and study its characteristic speeds in "trumpet" coordinates.

FIG. 16: The fitting of the orbital radius R vs. orbital frequency Ωin the NR coordinates for the $q = 1/10$ case. The solid (black), dashed (red) and dotted (blue) curves show the NR, fitting and ADM-TT PN evolutions, respectively. The fitting by using Eq. (12) is valid up to $M\Omega = 0.175$. In the NR evolution, the end point of the solid (black) curve corresponds to $R_{\rm Sch} = 2M$, and $M\Omega = 0.175$ is the NR orbital frequency around $R_{\rm Sch} = 3M$, assuming the NR coordinate system can be approximated by a "trumpet" stationary 1 + log slice of the Schwarzschild spacetime.

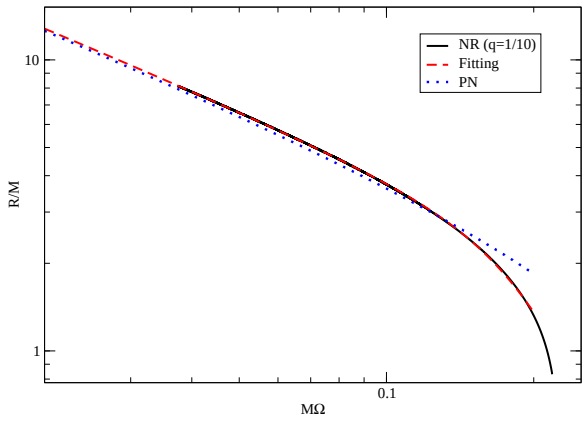

V. RESULTS

We obtain an approximation to $\Omega(T_{\rm NR})$ by integrating Eq. (8). We then obtain $R(T_{\rm NR})$ using Eq. (12) and the approximate $\Omega(T_{\rm NR})$. The initial orbital phase is not fixed, and we set it here such that the matching between the perturbative and numerical waveforms are maximized.

Note that part of the difference between the NR waveform and the perturbative waveforms is due to eccentricity in the numerical trajectories. This affects the time step of the orbital evolution through

$$dt = \left(\frac{d\Omega}{dt}\right)^{-1} d\Omega\,. \quad (15)$$

This may help explain why in the $q = 1/10$ case, we observe a slower time evolution in the fitting trajectory than the NR evolution.

FIG. 17: The fitting of the orbital radius R vs. orbital frequency Ω in the NR coordinates for the $q = 1/15$ case. The solid (black), dashed (red) and dotted (blue) curves show the NR, fitting and ADM-TT PN evolutions, respectively. The fitting by using Eq. (12) is valid up to $M\Omega = 0.17$. In the NR evolution, the end point of the solid (black) curve corresponds to $R_{\rm Sch} = 2M$, and $M\Omega = 0.17$ is the NR orbital frequency around $R_{\rm Sch} = 3M$, assuming the NR coordinate system can be approximated by a "trumpet" stationary 1 + log slice of the Schwarzschild spacetime.

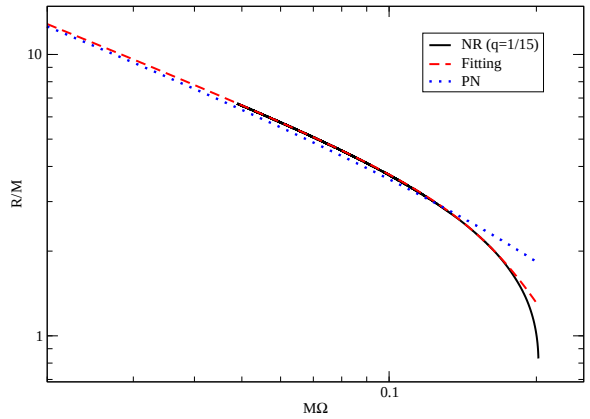

FIG. 18: The fitting of the orbital radius R vs. orbital frequency Ω in the NR coordinates for the $q = 1/100$ case. The solid (black), dashed (red) and dotted (blue) curves show the NR, fitting and ADM-TT PN evolutions, respectively. The fitting by using Eq. (12) is valid up to $M\Omega = 0.15$. In the NR evolution, the end point of the solid (black) curve corresponds to $R_{\rm Sch} = 2M$, and $M\Omega = 0.15$ is the NR orbital frequency around $R_{\rm Sch} = 3M$, assuming the NR coordinate system can be approximated by a "trumpet" stationary 1 + log slice of the Schwarzschild spacetime.

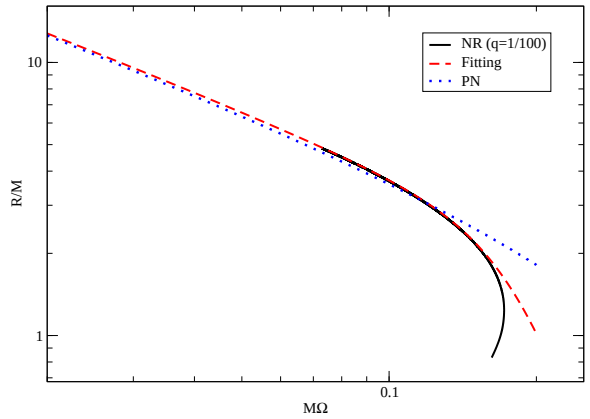

In order to generate the final plunge trajectory and regularize the behavior of the source near the horizon in the SRWZ formalism [22], we attach the model for the trajectories to a plunging geodesic in a continuous way. To do this, we choose a matching radius $R_{\rm M} \sim 3M$ in Schwarzschild coordinates (the light ring) and then determine the energy and angular momentum of the trajectory at that point. We then complete the trajectory from $R \sim R_{\rm M}$ to $R \sim 2M$ using the geodesic with the same energy and angular momentum. We note that the waveform evolution after the particle crosses the light ring is dominated by the quasi-normal ringing of the BH [55].

When we set the matching radius to $R_{\rm M} = 3M$, we find that the energy E and angular momentum L in the Schwarzschild coordinates are given by

$$\begin{aligned} E &= \frac{1}{3}\, u^t \,, \\ L &= 9\, M^2\, u^\phi \,, \end{aligned} \tag{16}$$

where $u^\mu = dx^\mu/d\tau$ is the four velocity, and we focus on equatorial orbits. To evaluate u^t in the above equation, we use

$$g_{\mu\nu} u^\mu u^\nu = -1 \,, \tag{17}$$

where $g_{\mu\nu}$ denotes the Schwarzschild metric, and at $R_{\rm M} = 3M$ this becomes

$$\begin{aligned} u^t = \Bigg[& \frac{1}{3} - 3(\dot{R}_{\rm Sch}(T_{\rm Sch}))^2 \\ & -9\, M^2 (\dot{\Phi}_{\rm Sch}(T_{\rm Sch}))^2 \Bigg]^{-1/2} . \end{aligned} \tag{18}$$

Here, $\dot{R}_{\rm Sch} = u^r/u^t = dR_{\rm Sch}/dT_{\rm Sch}$ and $\dot{\Phi}_{\rm Sch} = u^\phi/u^t = d\Phi_{\rm Sch}/dT_{\rm Sch}$ are the velocity components obtained from the numerical data after the coordinate transformation from the "trumpet" coordinates to the Schwarzschild coordinates. We also use Eq. (17) to calculate u^t in the source term of the SRWZ formalism.

In the SRWZ formalism, the gravitational waveforms at a sufficiently distant location $R_{\rm Obs}$ is given by

$$\begin{aligned} \frac{R_{\rm Obs}}{M}\,(h_+ - i\, h_\times) = & \sum_{\ell m} \frac{\sqrt{(\ell-1)\ell(\ell+1)(\ell+2)}}{2M} \\ & \times \left(\Psi^{\rm (even)}_{\ell m} - i\, \Psi^{\rm (odd)}_{\ell m} \right) {}_{-2}Y_{\ell m} \,. \end{aligned} \tag{19}$$

We use the normalized waveform, i.e., the expression in the right hand side of the above equation to calculate the wave amplitude.

On the other hand, to convert the NR ψ_4, which is extrapolated to infinity via Eq. (2), to the waveform h, we use the "pyGWAnalysis" code in EinsteinToolkit [28] (see Ref. [56] for details). Then, we calculate the match between the NR and SRWZ waveforms in the advanced LIGO (Zero Det, High Power) noise curve [57]. We note that, unlike in the overlap calculation used in Ref. [58], here we consider a match maximized over time and phase, which has the effect that errors in the waveforms can be hidden by the match. In Table V, we summarize the match for the three mass ratios. In the following subsections, we treat each mass ratio case separately.

A. The $q = 1/100$ case

For the $q = 1/100$ case, the fitting formulas in Eqs. (8) and (12) are valid for orbital frequencies up to $M\Omega = 0.15$

TABLE V: The match between the NR and SRWZ waveforms for various total masses using the advanced LIGO noise curve. For the smaller masses, the entire waveform is in the advanced LIGO band, while for the larger masses, only the final ringdown part of the waveform is in band. For these larger masses, we integrate over frequencies $f \geq 10$Hz. Here we only used the ($\ell = 2$, $m = 2$) mode to calculate the match.

Total mass ($M_\odot$)	$q = 1/10$	$q = 1/15$	$q = 1/100$
100	0.983019	0.982900	0.995162
200	0.992766	0.992704	0.995216
300	0.996219	0.996514	0.995486
400	0.996781	0.997734	0.995513
500	0.996844	0.997973	0.995474

in the "trumpet" coordinates. Here, we extend them beyond $M\Omega = 0.15$ by attaching these trajectories to a plunging geodesic at $R_{\rm M}$ (as explained above).

Ideally, we would like to use as much of the fitting trajectory as possible. However, when attempting to use the fitting trajectory to calculate the 4-velocity at small radii, we can not evaluate u^t for $R_{\rm Sch} \leq 2.12M$ from Eq. (17) because the approximation that the background metric is Schwarzschild in "trumpet" coordinates breaks down and the vector $(1, \dot{R}_{\rm Sch}, 0, \dot{\Phi}_{\rm Sch})$ becomes spacelike in the background metric (but not in the numerical metric). This breakdown can be thought to arise from the interaction of the singular part of the conformal factor due to the smaller BH (when it is close to horizon of the larger one) with the singular part of the conformal factor due to the larger BH. This, in turn, changes $\tilde{\Gamma}^i$, and therefore the gauge, when the two BHs approach each other. Also, since we see some delay in the phase evolution for a small matching radius near the horizon, we set $R_{\rm M} \sim 3M$ for the start of the geodesic approximation. At this matching radius, E and L for the Schwarzschild geodesic are evaluated from the orbital separation and three velocity using Eq. (16). We find

$$\begin{aligned} E &= 0.93942436\,, \\ L/M &= 3.46184226\,. \end{aligned} \tag{20}$$

In the SRWZ formalism, we set the non-dimensional spin parameter $\alpha = 0.033$ (see Table II). Although this value is obtained in the NR simulation, we can also obtain it from an empirical formula [59].

We next calculate the match in the advanced LIGO noise curve. For the integration in the frequency domain, we consider gravitational wave frequencies $M\Omega_{22} \geq 0.15$. For a total mass $M = 484M_\odot$, where we have the lower frequency cut off (corresponding to the start of the numerical waveform) at $f_{\rm low} = 10.01$Hz, the match between the NR and SRWZ waveforms is

$$\mathcal{M}_{22} = 0.995477\,, \tag{21}$$

for the ($\ell = 2$, $m = 2$) mode. The amplitude and phase evolutions for the NR and SRWZ waveforms are shown in Fig. 19. To obtain this figure, we translated the waveforms so that the maximum in the amplitude occurs at $t = 0$ and used the freedom in the phase to set it to zero at $t = -75M$.

FIG. 19: The amplitude (TOP) and phase (BOTTOM) of the ($\ell = 2$, $m = 2$) mode of h for the $q = 1/100$ case. The waveforms were translated in time such that the maximum in the amplitude occurs at $t = 0$ and the phases were adjusted by a constant offset such that $\phi = 0$ at $t = -75M$. The solid (black) and dashed (red) curves show the NR and SRWZ waveforms, respectively.

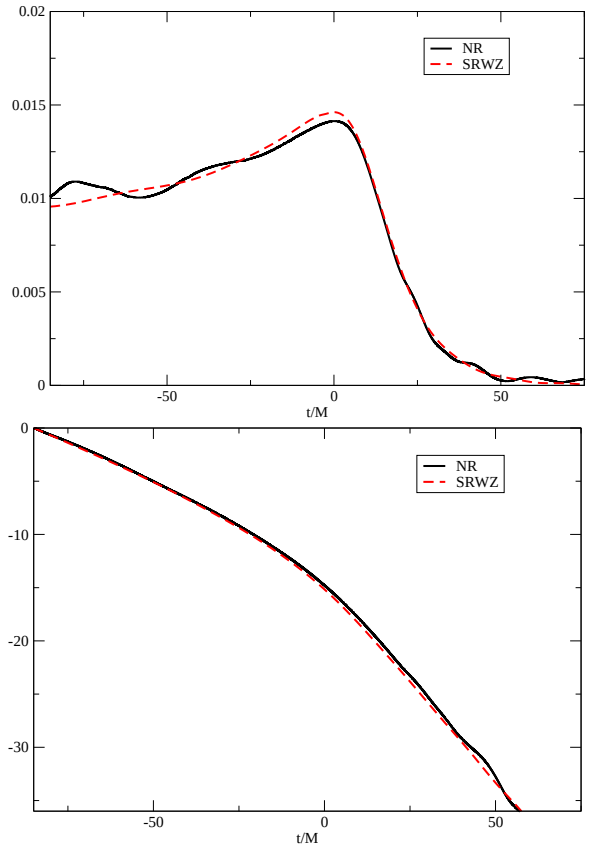

The ($\ell = 2$, $m = 1$) mode of h is the leading contribution from the odd parity in the RWZ calculation. The amplitude and phase evolutions for this mode are shown in Fig. 20. After adding a time translation so that the maximum in the amplitude occurs at $t = 0$ and a phase translation so that the phase $\phi = 0$ is zero at $t = -75M$, we still see a small difference between the phases. For a total mass of $M = 242M_\odot$ (this mass is chosen such that the lowest frequency is just in the advanced LIGO band $f_{\rm low} = 10.01$Hz), the match between the NR and SRWZ waveforms for this mode is given by

$$\mathcal{M}_{21} = 0.957966\,. \tag{22}$$

For the ($\ell = 3$, $m = 3$) mode of h, the amplitude and phase evolutions are shown in Fig. 21. For $M = 726M_\odot$ (mass chosen so that $f_{\rm low} = 10.01$Hz), the match for this

mode is

$$\mathcal{M}_{33} \;=\; 0.993895\,. \tag{23}$$

FIG. 20: The amplitude (TOP) and phase (BOTTOM) of the ($\ell = 2$, $m = 1$) mode of h for the $q = 1/100$ case. The waveforms were translated in time such that the maximum in the amplitude occurs at $t = 0$ and the phases were adjusted by a constant offset such that $\phi = 0$ at $t = -75M$. The solid (black) and dashed (red) curves show the NR and SRWZ waveforms, respectively.

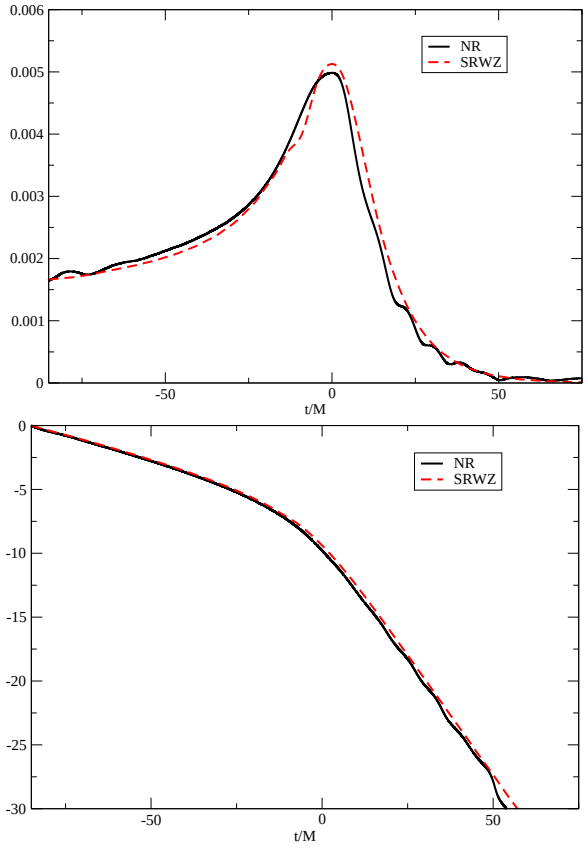

B. The $q = 1/10$ case

For the $q = 1/10$ case, the fitting formulae is valid up to larger orbital frequencies than for the $q = 1/100$ case. Nevertheless, u^t can not be evaluated for $R_{\rm Sch} \leq 2.26M$ from Eq. (17). Therefore, we need to start the geodesic approximation at radii larger than this, and again we set the matching radius $R_{\rm M} \sim 3M$. We find that the energy and angular momentum for the Schwarzschild geodesic are given by

$$\begin{aligned} E \;&=\; 1.02546489\,, \\ L/M \;&=\; 3.95926146\,, \end{aligned} \tag{24}$$

at the matching radius. Not that the energy is $E > 1$ because we simply project the orbital quantities on the Schwarzschild spacetime by using Eqs. (16) and (17) (this is a strong indication that the motion of the $q = 1/10$ binary is non-geodesic even close to the larger BH). In the SRWZ formalism, we set the non-dimensional spin parameter to $\alpha = 0.26$, consistent with the measured spin from the numerical simulation (see Table II).

FIG. 21: The amplitude (TOP) and phase (BOTTOM) of the ($\ell = 3$, $m = 3$) mode of h for the $q = 1/100$ case. The waveforms were translated in time such that the maximum in the amplitude occurs at $t = 0$ and the phases were adjusted by a constant offset such that $\phi = 0$ at $t = -75M$. The solid (black) and dashed (red) curves show the NR and SRWZ waveforms, respectively.

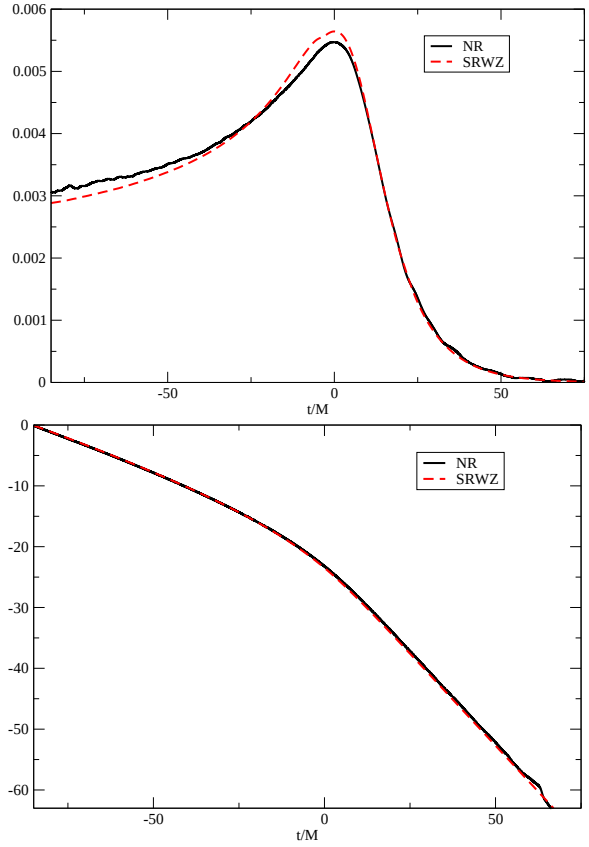

The amplitude and phase evolutions of the ($\ell = 2$, $m = 2$) mode of h are shown in Fig. 22. While the phases of the NR and SRWZ waveforms are in good agreement, there are relatively large differences in the amplitudes both for the inspiral and merger phases. We will discuss the amplitude differences in more detail in Sec. V D.

We consider the match calculation for $M\Omega_{22} \geq 0.075$ and total mass $M = 242M_\odot$, i.e., the lower frequency cut off at $f_{\rm low} = 10.01$Hz. In this case the match between the NR and SRWZ waveforms is

$$\mathcal{M}_{22} \;=\; 0.994669\,, \tag{25}$$

for the ($\ell = 2$, $m = 2$) mode in the advanced LIGO noise curve.

The amplitude and phase evolutions for the ($\ell = 2$, $m = 1$) mode of h are shown in Fig. 23., For $M =$

FIG. 22: The amplitude (TOP) and phase (BOTTOM) of the ($\ell = 2, m = 2$) mode of h for the $q = 1/10$ case. The waveforms were translated in time such that the maximum in the amplitude occurs at $t = 0$ and the phases were adjusted by a constant offset such that $\phi = 0$ at $t = -830M$. The solid (black) and dashed (red) curves show the NR and SRWZ waveforms, respectively.

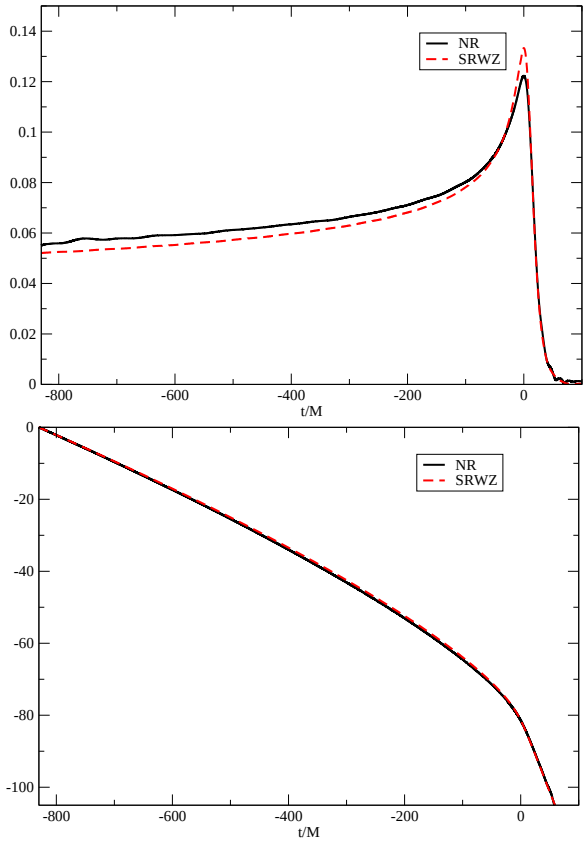

FIG. 23: The amplitude (TOP) and phase (BOTTOM) of the ($\ell = 2, m = 1$) mode of h for the $q = 1/10$ case. The waveforms were translated in time such that the maximum in the amplitude occurs at $t = 0$ and the phases were adjusted by a constant offset such that $\phi = 0$ at $t = -830M$. The solid (black) and dashed (red) curves show the NR and SRWZ waveforms, respectively.

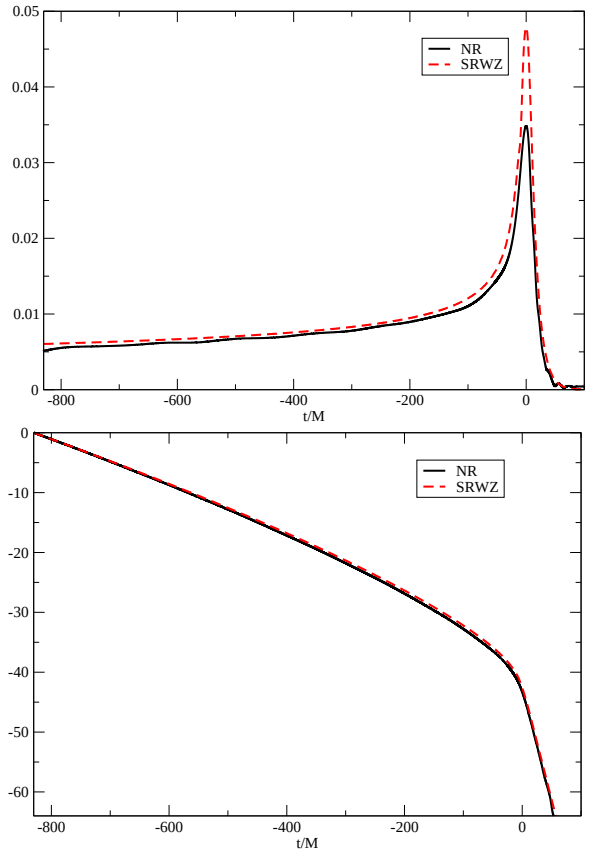

$121M_\odot$ ($f_{\rm low} = 10.01$Hz), the match for this mode is

$$\mathcal{M}_{21} \;=\; 0.989382\,. \qquad (26)$$

The amplitude and phase evolutions for the ($\ell = 3, m = 3$) mode of h are shown in Fig. 24. For $M = 363M_\odot$ ($f_{\rm low} = 10.01$Hz), the match for this mode is

$$\mathcal{M}_{33} \;=\; 0.987414\,. \qquad (27)$$

We have a similar mismatch in the ($\ell = 2, m = 1$) and ($\ell = 3, m = 3$) modes.

We note that although the ($\ell = 2, m = 1$) and ($\ell = 3, m = 3$) modes have a slightly large mismatch ($1 - \mathcal{M}$), these modes are the sub-dominant contributions to the gravitational wave. The maximum amplitudes are ~ 0.12, 0.035 and 0.04 for the ($\ell = 2, m = 2$), ($\ell = 2, m = 1$) and ($\ell = 3, m = 3$) modes, respectively. Therefore, we find that from a rough estimation the contribution of the mismatch for each mode are almost same in the gravitational wave.

Also, as discussed in Ref. [22], unlike the case of $q = 1/100$, here the spin corrections in the SRWZ formalism are important for obtaining the correct ringdown phase. We see that the correct ringdown frequency was obtained by comparing the slope of the phase evolution in Figs. 22, 23 and 24.

C. The $q = 1/15$ case

For the $q = 1/15$ case, the fitting formula is valid up to larger orbital frequencies than for the $q = 1/100$ case. Here too, we can not calculate u^t for $R_{\rm Sch} \leq 2.21M$ from Eq. (17), and again we use the geodesic approximation and a matching radius $R_{\rm M} \sim 3M$. We find that the energy and angular momentum are given by

$$\begin{aligned} E &= 0.985372666\,, \\ L/M &= 3.74699937\,. \end{aligned} \qquad (28)$$

In the SRWZ formalism, we set the non-dimensional spin parameter $\alpha = 0.19$, consistent with the numerical results (see Table II).

FIG. 24: The amplitude (TOP) and phase (BOTTOM) of the ($\ell = 3, m = 3$) mode of h for the $q = 1/10$ case. The waveforms were translated in time such that the maximum in the amplitude occurs at $t = 0$ and the phases were adjusted by a constant offset such that $\phi = 0$ at $t = -830M$. The solid (black) and dashed (red) curves show the NR and SRWZ waveforms, respectively.

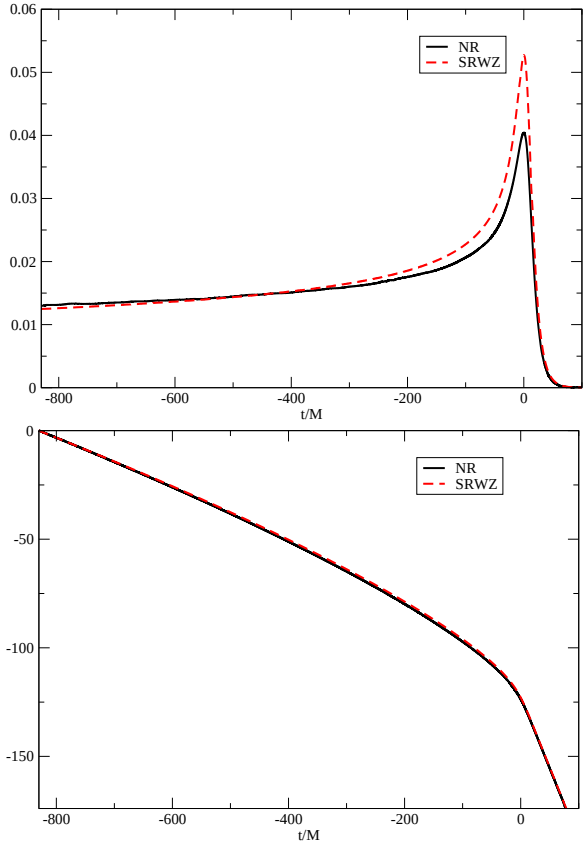

FIG. 25: The amplitude (TOP) and phase (BOTTOM) of the ($\ell = 2, m = 2$) mode of h for the $q = 1/15$ case. The waveforms were translated in time such that the maximum in the amplitude occurs at $t = 0$ and the phases were adjusted by a constant offset such that $\phi = 0$ at $t = -600M$. The solid (black) and dashed (red) curves show the NR and SRWZ waveforms, respectively.

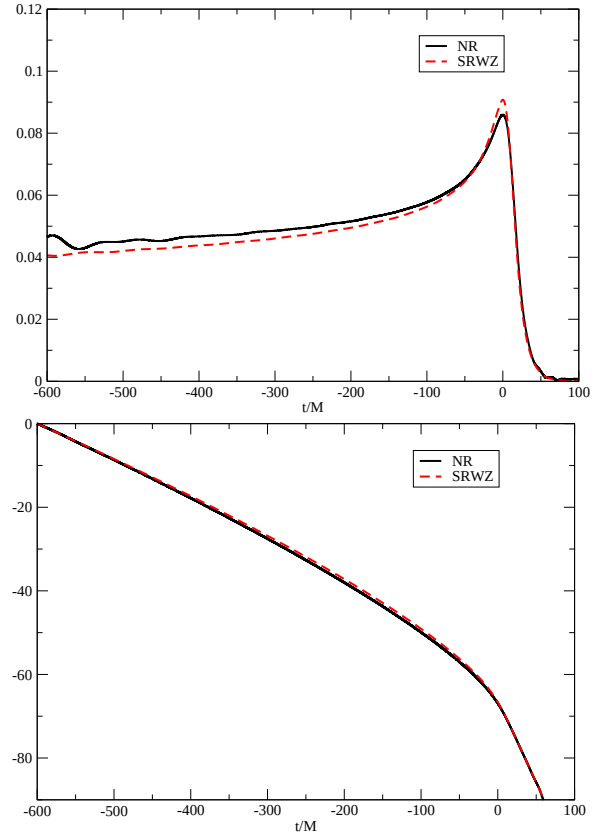

The amplitude and phase evolutions of the ($\ell = 2$, $m = 2$) mode of h are shown in Fig. 25. The match for $M\Omega_{22} \geq 0.09$ with a total mass of $M = 290M_\odot$ ($f_{\rm low} = 10.02$Hz) is

$$\mathcal{M}_{22} \;=\; 0.996039\,, \tag{29}$$

using the advanced LIGO noise curve.

The amplitude and phase evolutions for the ($\ell = 2$, $m = 1$) mode of h are shown in Fig. 26. For $M = 145M_\odot$ ($f_{\rm low} = 10.02$Hz), the match for this mode is

$$\mathcal{M}_{21} \;=\; 0.989005\,. \tag{30}$$

The amplitude and phase evolutions for the ($\ell = 3$, $m = 3$) mode of h are shown in Fig. 27. For $M = 435M_\odot$ ($f_{\rm low} = 10.01$Hz), the match for this is

$$\mathcal{M}_{33} \;=\; 0.986921\,. \tag{31}$$

As was seen in the $q = 1/10$ case, we have a somewhat large mismatch for the sub-dominant ($\ell = 2$, $m = 1$) and ($\ell = 3$, $m = 3$) modes.

D. Amplitude differences

Here, we focus on the amplitude of the ($\ell = 2$, $m = 2$) mode of h obtained using NR and the SRWZ formalism. In Fig. 28, we show the amplitude difference between the NR and SRWZ waveforms for the $q = 1/10$ case. There is a large ($\sim 10\%$) difference in the amplitudes both in the inspiral and merger phases.

To understand this difference, we compare the amplitude differences between the NR and SRWZ waveforms for the other mass ratio cases. Using the following definition for the amplitude difference,

$$\delta A_{22} = |A_{22}^{\rm (SRWZ)} - A_{22}^{\rm (NR)}|\,, \tag{32}$$

we find that the amplitude differences for the $q = 1/10$ and $q = 1/15$ cases around the maximum amplitude obey

$$\begin{aligned} \delta A_{22}^{(q=1/10)} &\sim 2.3 \times \delta A_{22}^{(q=1/15)} \\ &\sim 1.41^{2.42} \times \delta A_{22}^{(q=1/15)}\,, \end{aligned} \tag{33}$$

where 1.41 is the ratio of the symmetric mass ratios η.

FIG. 26: The amplitude (TOP) and phase (BOTTOM) of the ($\ell = 2, m = 1$) mode of h for the $q = 1/15$ case. The waveforms were translated in time such that the maximum in the amplitude occurs at $t = 0$ and the phases were adjusted by a constant offset such that $\phi = 0$ at $t = -600M$. The solid (black) and dashed (red) curves show the NR and SRWZ waveforms, respectively.

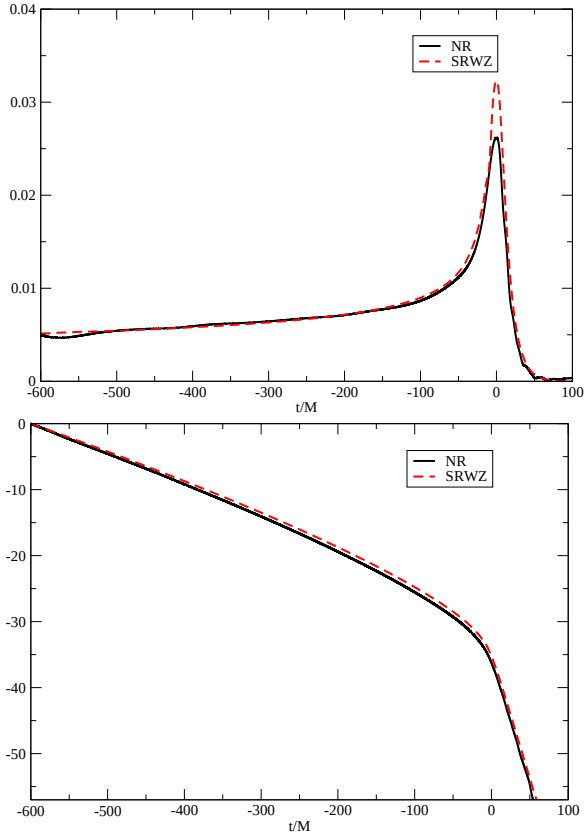

FIG. 27: The amplitude (TOP) and phase (BOTTOM) of the ($\ell = 3, m = 3$) mode of h for the $q = 1/15$ case. The waveforms were translated in time such that the maximum in the amplitude occurs at $t = 0$ and the phases were adjusted by a constant offset such that $\phi = 0$ at $t = -600M$. The solid (black) and dashed (red) curves show the NR and SRWZ waveforms, respectively.

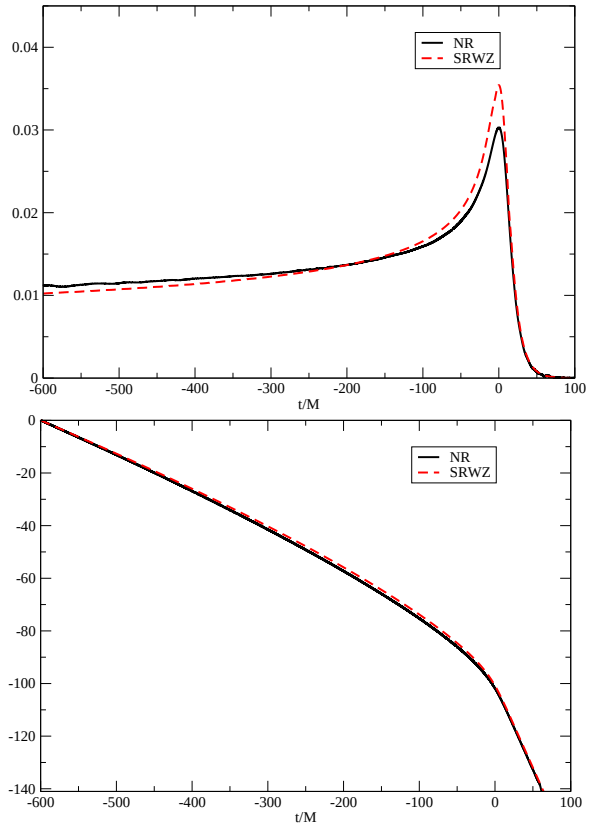

Figure 29 shows the amplitude differences (note that $t = 0$ denotes the time of the maximum amplitude) for $q = 1/10$ and $q = 1/15$. We see that the amplitude difference before merger is proportional to the ratio of the symmetric mass ratio. This behavior is different from our previous analysis in Ref. [22], where we directly used the NR trajectories in the perturbative calculation of the waveforms, and found that the amplitude difference in the inspiral phase scales like η^2. Since the fitting formula is based on the quasicircular evolution, any eccentricity of the orbit may create amplitude differences during the inspiral phase.

Figure 30 shows the amplitude differences both for the $q = 1/10$ and $q = 1/100$ waveforms. Near the maximum amplitude, we find that the amplitude differences scale like

$$\begin{aligned} \delta A_{22}^{(q=1/10)} &\sim 21.5 \times \delta A_{22}^{(q=1/100)} \\ &\sim 8.43^{1.44} \times \delta A_{22}^{(q=1/100)}, \end{aligned} \tag{34}$$

where 8.43 is the ratio of the symmetric mass ratio. Note that this rescaling does not capture the behavior

FIG. 28: The amplitude difference of the ($\ell = 2$, $m = 2$) mode of h for the $q = 1/10$ case. Here, the difference is normalized by the NR amplitude. We see $\sim 10\%$ difference in the inspiral and merger phases.

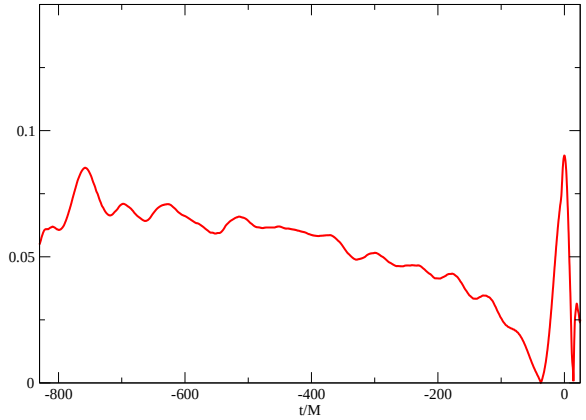

of the amplitude differences during the inspiral phase. Although it is difficult to obtain any exact relation between the amplitude differences during the inspiral (pos-

FIG. 29: The amplitude difference δA_{22} of the ($\ell = 2$, $m = 2$) mode of h for the $q = 1/10$ and $1/15$ cases.

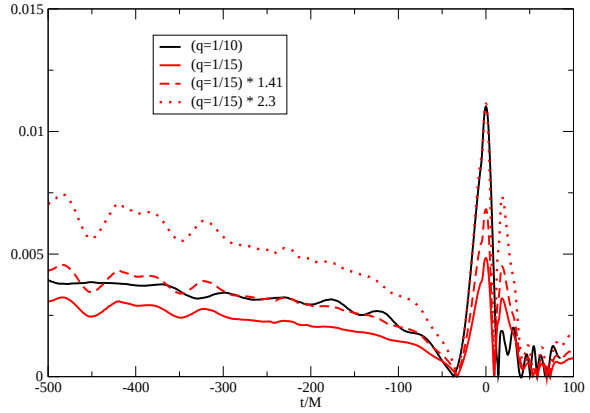

sibly due to effects of eccentricity), we do observe nonlinear effects in the amplitude difference between the NR and SRWZ waveforms around the maximum amplitude, which we infer from the fact that the amplitude difference scales nonlinearly with the mass ratio.

FIG. 30: The amplitude difference δA_{22} of the ($\ell = 2$, $m = 2$) mode of h for the $q = 1/10$ and $1/100$ cases.

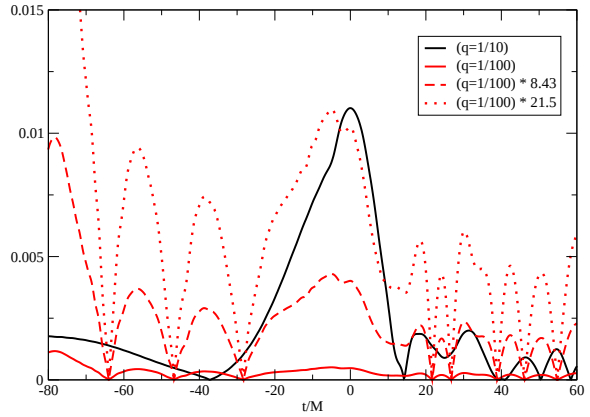

Figure 31 shows the amplitude differences both for the $q = 1/15$ and $q = 1/100$ cases. Near the maximum amplitude, we find that the amplitude differences scale like

$$\begin{aligned} \delta A_{22}^{(q=1/15)} &\sim 9.5 \times \delta A_{22}^{(q=1/100)} \\ &\sim 5.98^{1.26} \times \delta A_{22}^{(q=1/100)} , \end{aligned} \tag{35}$$

where 5.98 is the ratio of the symmetric mass ratios. Again, we see the similar behavior to $q = 1/10$ and $q = 1/100$ comparison.

We note that the C transformation in Eq. (13) also affects the amplitude difference. As seen in Fig. 32, if we directly use the orbital radius $R_{\rm NR}$ to calculate the waveforms, we obtain an even larger amplitude than that obtained using the corrected orbital radius $R_{\rm Log}$. This behavior is expected based on the fact that while the orbital radius is larger, the orbital frequency remains the same. Although the orbital radius $R_{\rm NR}$ gives a similar amplitude to the NR waveform in the initial inspiral part, we have a much larger amplitude in the merger phase.

FIG. 31: The amplitude difference δA_{22} of the ($\ell = 2$, $m = 2$) mode of h for the $q = 1/15$ and $1/100$ cases.

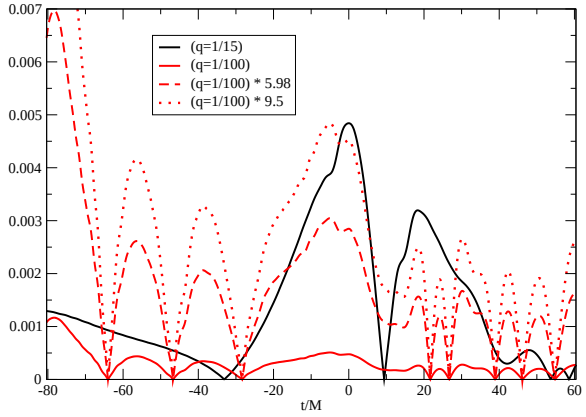

FIG. 32: The amplitude of the ($\ell = 2$, $m = 2$) mode of h for the $q = 1/10$ case. We have set the maximum amplitudes at $t = 0$ by the time translation. The solid (black), dashed (red) and dotted (blue) curves show the waveforms from the NR, SRWZ and SRWZ without the C transformation in Eq. (12), respectively.

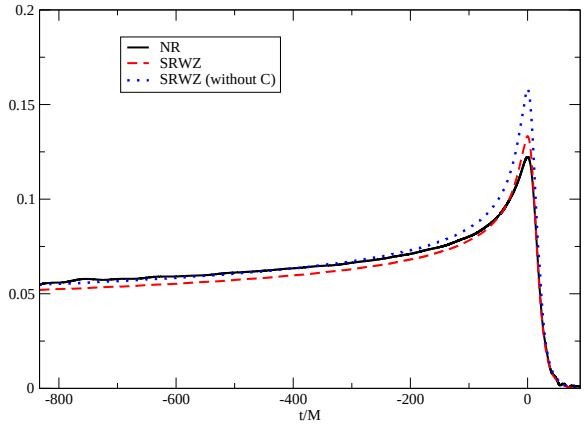

VI. DISCUSSION

In the first paper of this series [22] we established that perturbation theory of BHs in the extreme-mass-ratio expansion $q = m_1/m_2 \ll 1$, as in Eq. (6), can faithfully represent an approximation to the full numerical simulations, if we provide the full numerical relative trajectory of the holes as a function of time. In this second paper we proceed to model these trajectories using full numerical simulations and a parametrized extension of 3.5 PN quasi-adiabatic evolutions, Eqs. (8) and (12). This form of the expansion allows us to incorporate the PN trajectory at large distances and smoothly fit to the full

numerical ones up to separations as small as $R_{\rm Sch} = 3M$, at which point we can describe the subsequent trajectory by a Schwarzschild plunging geodesic. In this approximation, we set the values of the energy E and angular momentum L of the geodesic to those of the previously fitted trajectory evaluated at $R_{\rm Sch} = 3M$.

Once we verified the procedure for each of the test runs, i.e. for $q = 1/10$, $1/15$ and $1/100$, we obtain an expression for the fitting parameters as a function of q, as given in Eqs. (11). The other piece of information needed by the perturbative approach, in addition to the relative trajectory, are the mass and spin of the final BH formed after merger to provide the background metric. The spin and mass parameters for the SRWZ equation (6) can be estimated from empirical formulae [59, 60]. Note that this formula correctly predicted the remnant BH's mass and spin [16] for the three cases of mass ratio studied here.

The current study can be considered a successful proof of principle, and needs to be supplemented by a thorough set of runs in the intermediate mass ratio regime $0.01 \lesssim q \lesssim 0.1$ that start at separations where the PN approximation is still valid, i.e. $R \gtrsim 10M$ and go through the merger of the holes until the formation of a common horizon. The fitting formulae Eqs. (8) and (12) with Eqs. (11) should provide a good approximation within the fitting interval, but extrapolation to both the comparable masses or extreme mass ratio could quickly lose accuracy. The fitted tracks from our work can be compared to alternative approaches to the problem such as the EOB [61] and EOBNR [62, 63] and the final waveforms to direct phenomenological ones as given in Refs. [64, 65]. Our approach provides a complementary model for the intermediate mass- ratio regime to the above approaches, which mostly apply to the comparable-mass regime.

The extension of our approach to initially highly-spinning BHs can be done essentially through the same lines depicted here. Numerical simulations of highly spinning holes with small mass ratio are feasible [66], and the trajectories would already include the effect of the spins of both holes. The perturbative waveform calculation would use the Teukolsky formalism [67] and its second order extension [32]. Fitting formulae based on the extension of spinning PN trajectories with free parameter dependence on the mass ratio and effective spins should be used together with the final matching to plunging geodesics on an spinning background. The final remnant formulae for spinning binaries have already been proposed and fitted to available simulations [59, 60].

Acknowledgments

We thank Marcelo Ponce for providing the method to reduce the horizon mass loss required to make accurate simulations in the small mass ratio regime. We gratefully acknowledge the NSF for financial support from Grants No. PHY-0722315, No. PHY-0653303, No. PHY-0714388, No. PHY-0722703, No. DMS-0820923, No. PHY-0929114, PHY-0969855, PHY-0903782, and No. CDI-1028087; and NASA for financial support from NASA Grants No. 07-ATFP07-0158 and No. HST-AR-11763. Computational resources were provided by the Ranger cluster at TACC (Teragrid allocation TG-PHY060027N) and by NewHorizons at RIT.

Appendix A: Perturbative Equations in 1+log "trumpet" coordinates

In this work we used standard Schwarzschild coordinates to describe the background geometry and trajectory of the particle. To obtain the latter, we transformed the particle's location from the NR coordinates (assuming they were represented by $1 + \log$ trumpet coordinates of a Schwarzschild spacetime) into the standard Schwarzschild coordinates. It is also useful to see the form of the perturbative equations in these $1 + \log$ trumpet coordinates. This will help to assess potential regions where this approach might have limitations. In particular, since the trumpet coordinates are obtained in the late-time, stationary limit, wherever there still are strong dynamics, the approach could be inaccurate.

The generalized Regge-Wheeler-Zerilli equations for an arbitrary spherically symmetric background were found in Ref. [68]. Here, for the sake of simplicity, we use only the generalized Regge-Wheeler equation given in Ref. [69]. Formally, this equation can be written as

$$\begin{aligned} \ddot{\Phi}_{\rm RW} &= c_1\,\dot{\Phi}'_{\rm RW} + c_2\,\Phi''_{\rm RW} + c_3\,\dot{\Phi}_{\rm RW} \\ &\quad + c_4\,\Phi'_{\rm RW} + c_5\,\Phi_{\rm RW}\,, \end{aligned} \tag{A1}$$

where the dot and dash denote the time and radial derivatives, and the coefficients c_i ($i = 1, 2, 3, 4, 5$) are determined by the background metric.

For the background metric, we use the notation of [54], which has the form

$$\begin{aligned} ds^2 &= -(\alpha^2 - \beta^2)dt^2 + \frac{2\beta}{f}dtdr \\ &\quad + \frac{1}{f^2}dr^2 + R^2(d\theta^2 + \sin^2\theta d\phi^2)\,. \end{aligned} \tag{A2}$$

where α, β, f and R are functions of the radial coordinate r only. The coefficients c_i are then given by

$$\begin{aligned} c_1 &= 2\,f(r)\,\beta(r)\,, \\ c_2 &= (\alpha(r)^2 - \beta(r)^2)\,f(r)^2\,, \\ c_3 &= -(\beta(r)\,\alpha'(r) - \alpha(r)\,\beta'(r))\,\frac{f(r)}{\alpha(r)}\,, \\ c_4 &= \frac{f(r)^2}{\alpha(r)}\,(-2\,\alpha(r)\,\beta(r)\,\beta'(r) + \alpha(r)^2\,\alpha'(r) \\ &\quad + \beta(r)^2\,\alpha'(r)) + f(r)\,f'(r)\,(\alpha(r)^2 - \beta(r)^2)\,, \\ c_5 &= -\alpha(r)^2\,V(r)\,, \end{aligned} \tag{A3}$$

where V denotes the Regge-Wheeler potential,

$$V(r) \;=\; \frac{1}{R(r)^2}\left(\ell\,(\ell+1) - \frac{6\,M}{R(r)}\right). \qquad \text{(A4)}$$

When using the standard Schwarzschild coordinates, the above equation becomes the standard Regge-Wheeler equation. We note that for the Zerilli equation, we may set [68]

$$\begin{aligned} V(r) \;=\; & \frac{2}{R(r)^3(\lambda R(r)+3M)^2}\left[\lambda^2(\lambda+1)R(r)^3\right. \\ & \left.+3\lambda^2 M R(r)^2 + 9\lambda M^2 R(r) + 9M^3\right], \qquad \text{(A5)} \end{aligned}$$

where $\lambda = (\ell-1)(\ell+2)/2$.

We now consider the stationary 1 + log slices of the Schwarzschild spacetime in isotropic coordinates as an approximation to the NR coordinate system. As discussed in Ref. [54], the metric in this coordinate system can be obtained numerically.

Since the Schwarzschild metric is a solution of the vacuum General Relativity field equations, and since we are using a Killing lapse and shift [54], we have

$$\begin{aligned} \alpha(r) \;&=\; f(r)R'(r)\,, \\ \alpha(r)^2 - \beta(r)^2 \;&=\; 1 - \frac{2M}{R(r)}\,. \qquad \text{(A6)} \end{aligned}$$

From the stationary 1 + log slice condition, we have

$$Ce^{\alpha} \;=\; \left(\alpha^2 - 1 + \frac{2M}{R}\right)R^4\,, \qquad \text{(A7)}$$

where the constant C is determined by requiring that α' be regular at the "critical" point (where the denominator vanishes).

$$\frac{C}{M^4} \;=\; \frac{1}{128}(3+\sqrt{10})^3\exp(3-\sqrt{10})\,. \qquad \text{(A8)}$$

In isotropic coordinates we obtain

$$\alpha(r) \;=\; \frac{r\,R'(r)}{R(r)}\,. \qquad \text{(A9)}$$

Since the above equations are transcendental, we have to find numerical solutions. However, it is also useful to study their asymptotic behavior for large r. At large r we have,

$$\begin{aligned} R(r) \;&=\; r + M + \frac{1}{4}\frac{M^2}{r} - \frac{1}{8}\frac{C\,e}{r^3} + O(1/r^4)\,, \\ \alpha(r) \;&=\; 1 - \frac{M}{r} + \frac{1}{2}\frac{M^2}{r^2} - \frac{1}{4}\frac{M^3}{r^3} \\ &\quad + \left(\frac{1}{8} + \frac{1}{2}\frac{C}{M^4}\,e\right)\frac{M^4}{r^4} + O(1/r^5)\,, \qquad \text{(A10)} \end{aligned}$$

and the other two functions β and f can be found from Eqs. (A6).

Inserting these functions into Eqs. (A3), we find that the coefficients c_i are given by

$$\begin{aligned} c_1 \;&=\; \frac{2\sqrt{C\,e}}{r^2} + O(1/r^3)\,, \\ c_2 \;&=\; 1 - \frac{4\,M}{r} + \frac{17}{2}\frac{M^2}{r^2} - \frac{13\,M^3}{r^3} + \left(\frac{259}{16} + \frac{1}{4}\frac{C}{M^4}\,e\right)\frac{M^4}{r^4} + O(1/r^5)\,, \\ c_3 \;&=\; -2\,\frac{\sqrt{C\,e}}{r^3} + O(1/r^4)\,, \\ c_4 \;&=\; \frac{2\,M}{r^2} - \frac{17}{2}\frac{M^2}{r^3} + \frac{39}{2}\frac{M^3}{r^4} + \left(-\frac{259}{8} + \frac{3}{2}\frac{C}{M^4}\,e\right)\frac{M^4}{r^5} + O(1/r^6)\,, \\ c_5 \;&=\; \frac{\ell\,(\ell+1)}{r^2} - \frac{6\,M\,(1+\ell\,(\ell+1))}{r^3} + \frac{1}{2}\frac{M^2\,(84+37\,\ell\,(\ell+1))}{r^4} - \frac{1}{2}\frac{M^3\,(303+79\,\ell\,(\ell+1))}{r^5} \\ &\quad + \left(378 + \frac{1059}{16}\,\ell\,(\ell+1) + \frac{9}{4}\frac{C}{M^4}\,e\,\ell\,(\ell+1)\right)\frac{M^4}{r^6} + O(1/r^7)\,. \qquad \text{(A11)} \end{aligned}$$

If we set $C = 0$, the above coefficients are the same as those derived in the standard isotropic coordinates ($r_{\rm Sch} = r_{\rm Iso}(1+M/(2r_{\rm Iso}))^2$) for the Schwarzschild spacetime.

An important piece of information in setting up the grid refinements, particularly for the smaller BH is the perturbative potential [16]. Using the numerical method given in Ref. [54], we can obtain the potential term c_5. The "Regge-Wheeler" potentials for the standard Schwarzschild ($r_{\rm Sch}$), isotropic ($r_{\rm Iso}$), and the trumpet radial coordinates ($r_{\rm Log}$) (associated to the NR coordinates) are shown in Fig. 33, while the radial deriva-

tives of these potentials are shown in Fig. 34. In the trumpet coordinates, the radial coordinate covers up to $r_{\rm Log} = 0$, and α and R around $r_{\rm Log} = 0$ have the following forms [54].

$$\alpha(r_{\rm Log}) \sim r_{\rm Log}^{1.091}, \qquad R(r_{\rm Log}) \sim R_0 + \left(\frac{r_{\rm Log}}{1.181}\right)^{1.092}, \tag{A12}$$

where $R_0 \simeq 1.312M$. From the above equation, we see that the sphere corresponding to $r_{\rm Log} = 0$ has a finite circumference.

FIG. 33: The solid (black), dashed (blue), and dotted (red) curves show the standard Regge-Wheeler (TOP) and Zerilli (BOTTOM) potentials in the standard Schwarzschild coordinates, isotropic coordinates, and "trumpet" coordinates (which are the stationary 1 + log slices of the Schwarzschild spacetime in isotropic coordinates), respectively, for the $\ell = 2$ mode. Note that the location of the horizon is different in each system. $r_{\rm Sch} < 2M$, $r_{\rm Iso} < M/2$, $r_{\rm Log} < 0.8304M$ are inside the horizon. Note that the potential is finite at the horizon, and is always positive.

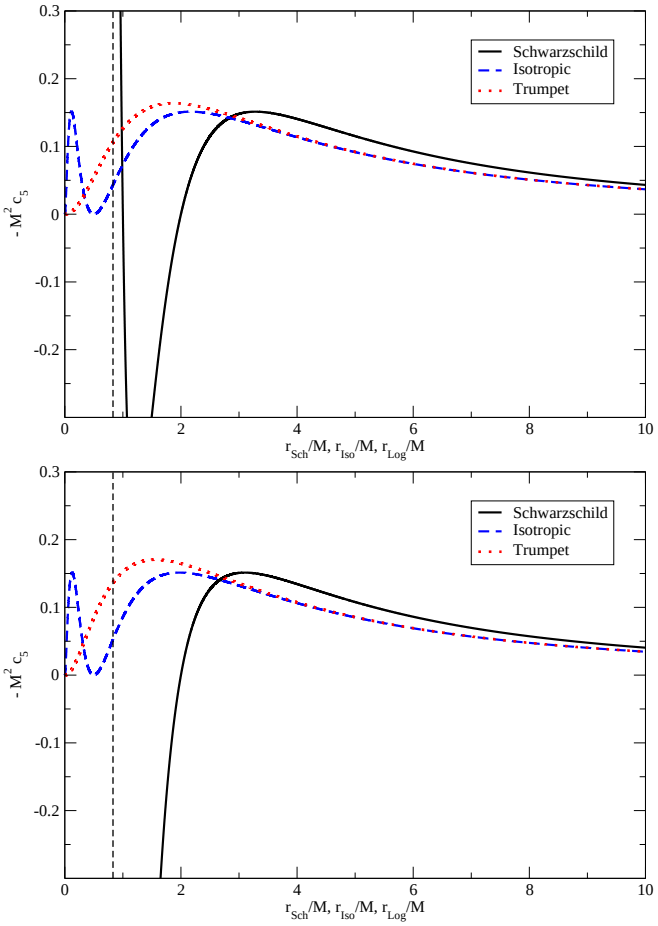

We observe that the differences between the "trumpet" and isotropic coordinates (outside the horizon), as determined by differences in the potentials, occurs in a region between the horizon and the maximum of the potential. This lends credence to the postulate that the main differences between the numerical coordinates and the "trumpet" coordinates lie in this region, as well. Indeed, as the two BHs approach each other, the conformal function W near the larger BH must change (since $W = 0$ at the location of the smaller BH, and varies smoothly outside the two punctures). Thus, as the small BH falls through the maximum of the potential, the coordinate system must become distorted in this important region. Therefore, we may expect that the assumption that the trajectory in the background spacetime is well described by assuming the coordinate radius is the trumpet radial coordinate breaks down. This may explain the need to match trajectories to plunging geodesics with slightly larger E and L values than one might expect (i.e. $E > 1$).

FIG. 34: The solid (black), dashed (blue), and dotted (red) curves show the radial derivative of the standard Regge-Wheeler (TOP) and Zerilli (BOTTOM) potentials in the standard Schwarzschild coordinates, isotropic coordinates, and "trumpet" coordinates, respectively, for the $\ell = 2$ mode. $r_{\rm Sch} < 2M$, $r_{\rm Iso} < M/2$, and $r_{\rm Log} < 0.8304M$ are inside the horizon. The vertical dashed lines denotes the location of the horizon in the "trumpet" coordinates.

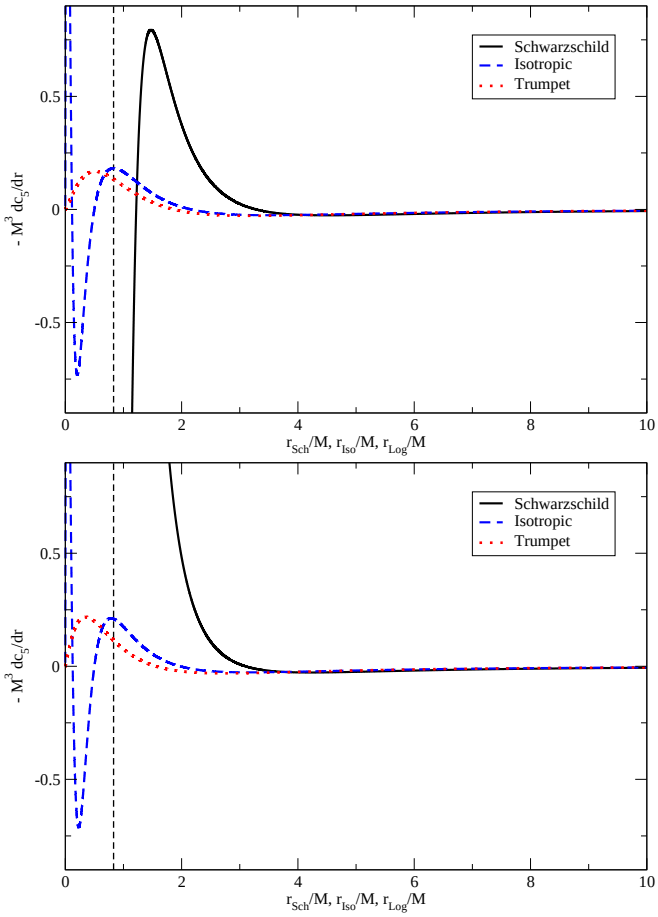

Another use of the perturbative potentials shown in Fig. 33 and, in particular, its radial derivative shown in Fig. 34, is to guide the set up of the numerical grid structure near the BHs [16]. To set up the mesh refinement levels, we chose grids that cover the region between the zeros of the derivative of the potential. The idea is that we need to model the curvature and the gravitational radiation emitted by the small BH (which drives the merger, and hence the physics). At the zeros of the derivative of the potentials, the variations are minimized. Furthermore the separations between zeros increases, naturally leading to a choice of small-width, high resolution grids between the first zeros, one step lower in resolution between the second two, followed by a sequence of coarser grids.

In order to understand one of the main features of the wave propagation, we also calculate the ingoing and outgoing characteristic speeds for this system [70]. Using our definition of the metric, these are given by

$$\begin{aligned} c_+ &= f(r)\,(\alpha(r)-\beta(r))\,, \\ c_- &= -f(r)\,(\alpha(r)+\beta(r))\,. \end{aligned} \tag{A13}$$

Figure 35 shows the radial dependence in the trumpet coordinates. Note that inside the horizon, ($r_{\rm Log} = 0.8304M$), both speeds remain negative and that the outgoing characteristic speed vanishes precisely at the horizon. Both modes reach their asymptotic speeds (± 1), at much larger radii.

FIG. 35: The ingoing and outgoing characteristic speeds. We see that $c_+ = 0$ but c_- is finite at the horizon (denoted by the vertical dashed line, $r_{\rm Log} = 0.8304M$), and that both speeds are negative inside the horizon. The thin curves show the characteristic speeds for the perturbation in the isotropic coordinates. Note that in this latter case, both speeds are zero on the horizon ($r_{\rm Iso} = M/2$).

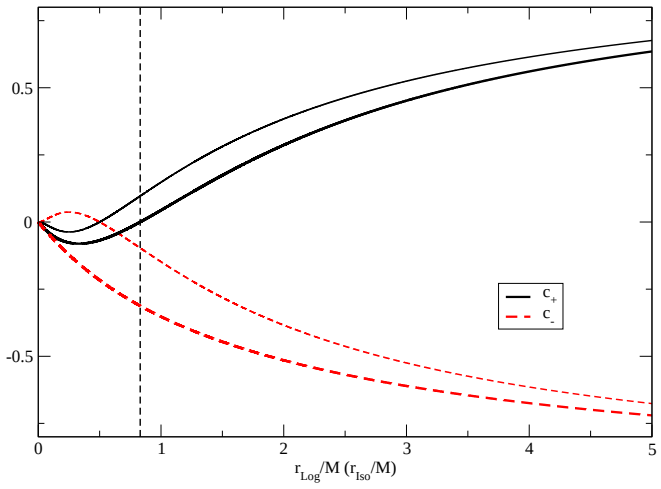

It is interesting to observe the differences between the usual isotropic coordinates in the standard Schwarzschild slicing and the "trumpet" coordinates. The initial data are in isotropic coordinates, therefore these differences are indicative of how the background has to change from the initial slice to the eventual "trumpet" slice.

[1] F. Pretorius, Phys. Rev. Lett. **95**, 121101 (2005), gr-qc/0507014.
[2] M. Campanelli, C. O. Lousto, P. Marronetti, and Y. Zlochower, Phys. Rev. Lett. **96**, 111101 (2006), gr-qc/0511048.
[3] J. G. Baker, J. Centrella, D.-I. Choi, M. Koppitz, and J. van Meter, Phys. Rev. Lett. **96**, 111102 (2006), gr-qc/0511103.
[4] B. Aylott et al., Class. Quant. Grav. **26**, 165008 (2009), 0901.4399.
[5] M. Campanelli, C. O. Lousto, Y. Zlochower, and D. Merritt, Astrophys. J. **659**, L5 (2007), gr-qc/0701164.
[6] J. A. González, M. D. Hannam, U. Sperhake, B. Brugmann, and S. Husa, Phys. Rev. Lett. **98**, 231101 (2007), gr-qc/0702052.
[7] M. Campanelli, C. O. Lousto, Y. Zlochower, and D. Merritt, Phys. Rev. Lett. **98**, 231102 (2007), gr-qc/0702133.
[8] C. O. Lousto and Y. Zlochower (2011), 1108.2009.
[9] Y. Sekiguchi and M. Shibata, Astrophys. J. **737**, 6 (2011), 1009.5303.
[10] C. O. Lousto and Y. Zlochower, Phys. Rev. **D77**, 024034 (2008), 0711.1165.
[11] M. Campanelli, C. O. Lousto, and Y. Zlochower, Phys. Rev. **D79**, 084012 (2009), 0811.3006.
[12] R. Owen, Phys. Rev. **D81**, 124042 (2010), 1004.3768.
[13] M. Campanelli, C. O. Lousto, and Y. Zlochower, Phys. Rev. **D74**, 041501(R) (2006), gr-qc/0604012.
[14] M. Ponce, C. Lousto, and Y. Zlochower, Class. Quant. Grav. **28**, 145027 (2011), 1008.2761.
[15] M. Shibata and H. Yoshino, Phys. Rev. **D81**, 104035 (2010), 1004.4970.
[16] C. O. Lousto and Y. Zlochower, Phys. Rev. Lett. **106**, 041101 (2011), 1009.0292.
[17] U. Sperhake, V. Cardoso, C. D. Ott, E. Schnetter, and H. Witek (2011), 1105.5391.
[18] G. Lovelace, M. A. Scheel, and B. Szilagyi, Phys. Rev. **D83**, 024010 (2011), 1010.2777.
[19] G. Lovelace, M. Boyle, M. A. Scheel, and B. Szilagyi (2011), 1110.2229.
[20] T. Regge and J. A. Wheeler, Phys. Rev. **108**, 1063 (1957).
[21] F. J. Zerilli, Phys. Rev. **D2**, 2141 (1970).
[22] C. O. Lousto, H. Nakano, Y. Zlochower, and M. Campanelli, Phys. Rev. **D82**, 104057 (2010), 1008.4360.
[23] S. Brandt and B. Brügmann, Phys. Rev. Lett. **78**, 3606 (1997), gr-qc/9703066.
[24] M. Ansorg, B. Brügmann, and W. Tichy, Phys. Rev. **D70**, 064011 (2004), gr-qc/0404056.
[25] Y. Zlochower, J. G. Baker, M. Campanelli, and C. O. Lousto, Phys. Rev. **D72**, 024021 (2005), gr-qc/0505055.
[26] P. Marronetti, W. Tichy, B. Brügmann, J. Gonzalez, and U. Sperhake, Phys. Rev. **D77**, 064010 (2008), 0709.2160.
[27] Cactus Computational Toolkit home page: `http://www.cactuscode.org`.
[28] Einstein Toolkit home page: `http://einsteintoolkit.org`.
[29] E. Schnetter, S. H. Hawley, and I. Hawke, Class. Quantum Grav. **21**, 1465 (2004), gr-qc/0310042.
[30] J. Thornburg, Class. Quant. Grav. **21**, 743 (2004), gr-qc/0306056.
[31] O. Dreyer, B. Krishnan, D. Shoemaker, and E. Schnetter, Phys. Rev. **D67**, 024018 (2003), gr-qc/0206008.
[32] M. Campanelli and C. O. Lousto, Phys. Rev. **D59**, 124022 (1999), gr-qc/9811019.
[33] C. O. Lousto and Y. Zlochower, Phys. Rev. **D76**, 041502(R) (2007), gr-qc/0703061.
[34] M. Babiuc, B. Szilagyi, J. Winicour, and Y. Zlochower, Phys. Rev. **D84**, 044057 (2011), 1011.4223.
[35] C. Reisswig, N. T. Bishop, D. Pollney, and B. Szilagyi, Phys. Rev. Lett. **103**, 221101 (2009), 0907.2637.
[36] D. Pollney, C. Reisswig, E. Schnetter, N. Dorband, and P. Diener, Phys. Rev. **D83**, 044045 (2011), 0910.3803.
[37] B. Szilagyi, L. Lindblom, and M. A. Scheel, Phys. Rev. **D80**, 124010 (2009), 0909.3557.
[38] M. Alcubierre, B. Brügmann, P. Diener, M. Koppitz, D. Pollney, E. Seidel, and R. Takahashi, Phys. Rev. **D67**, 084023 (2003), gr-qc/0206072.
[39] M. Alcubierre et al. (2004), gr-qc/0411137.
[40] D. Müller and B. Brügmann, Class. Quant. Grav. **27**, 114008 (2010), 0912.3125.
[41] D. Müller, J. Grigsby, and B. Brügmann, Phys. Rev. **D82**, 064004 (2010), 1003.4681.
[42] E. Schnetter, Class. Quant. Grav. **27**, 167001 (2010), 1003.0859.
[43] D. Alic, L. Rezzolla, I. Hinder, and P. Mosta, Class. Quant. Grav. **27**, 245023 (2010), 1008.2212.
[44] J. A. González, U. Sperhake, B. Brugmann, M. Hannam, and S. Husa, Phys. Rev. Lett. **98**, 091101 (2007), gr-qc/0610154.
[45] C. O. Lousto, Class. Quant. Grav. **22**, S543 (2005), gr-qc/0503001.
[46] M. Boyle et al., Phys. Rev. **D76**, 124038 (2007), 0710.0158.
[47] P. Ajith, M. Boyle, D. A. Brown, S. Fairhurst, M. Hannam, I. Hinder, S. Husa, B. Krishnan, R. A. Mercer, F. Ohme, et al. (2007), 0709.0093.
[48] A. Ori and K. S. Thorne, Phys. Rev. **D62**, 124022 (2000), gr-qc/0003032.
[49] M. Kesden, Phys. Rev. **D83**, 104011 (2011), 1101.3749.
[50] I. MacDonald, S. Nissanke, and H. P. Pfeiffer, Class. Quant. Grav. **28**, 134002 (2011), 1102.5128.
[51] G. Schäfer, *Post-Newtonian methods: Analytic results on the binary problem* (Springer, New York, 2010), chap. 6, 0910.2857.
[52] B. J. Kelly, W. Tichy, M. Campanelli, and B. F. Whiting, Phys. Rev. **D76**, 024008 (2007), 0704.0628.
[53] W. Tichy, B. Brügmann, M. Campanelli, and P. Diener, Phys. Rev. **D67**, 064008 (2003), gr-qc/0207011.
[54] B. Brügmann, Gen. Rel. Grav. **41**, 2131 (2009), 0904.4418.
[55] T. Damour and A. Nagar, Phys. Rev. **D76**, 064028 (2007), 0705.2519.
[56] C. Reisswig and D. Pollney, Class. Quant. Grav. **28**, 195015 (2011), 1006.1632.
[57] *Advanced ligo anticipated sensitivity curves*, URL `https://dcc.ligo.org/cgi-bin/DocDB/ShowDocument?docid=2974`.
[58] M. Campanelli, C. O. Lousto, H. Nakano, and Y. Zlochower, Phys. Rev. **D79**, 084010 (2009), 0808.0713.
[59] C. O. Lousto, M. Campanelli, Y. Zlochower, and H. Nakano, Class. Quant. Grav. **27**, 114006 (2010), 0904.3541.

[60] L. Rezzolla, Class. Quant. Grav. **26**, 094023 (2009), 0812.2325.
[61] T. Damour and A. Nagar, Phys. Rev. **D79**, 081503 (2009), 0902.0136.
[62] Y. Pan et al., Phys. Rev. **D81**, 084041 (2010), 0912.3466.
[63] N. Yunes, A. Buonanno, S. A. Hughes, Y. Pan, E. Barausse, et al., Phys. Rev. **D83**, 044044 (2011), 1009.6013.
[64] L. Santamaria, F. Ohme, P. Ajith, B. Bruegmann, N. Dorband, et al., Phys. Rev. **D82**, 064016 (2010), 1005.3306.
[65] R. Sturani, S. Fischetti, L. Cadonati, G. Guidi, J. Healy, et al. (2010), 1012.5172.
[66] C. O. Lousto and Y. Zlochower, Phys. Rev. **D79**, 064018 (2009), 0805.0159.
[67] S. A. Teukolsky, Astrophys. J. **185**, 635 (1973).
[68] O. Sarbach and M. Tiglio, Phys. Rev. **D64**, 084016 (2001), gr-qc/0104061.
[69] E. Pazos et al., Class. Quant. Grav. **24**, S341 (2007), gr-qc/0612149.
[70] A. Zenginoglu, Class. Quant. Grav. **27**, 045015 (2010), 0911.2450.
[71] Marcelo Ponce, private communication